

JGR Atmospheres

RESEARCH ARTICLE

10.1029/2019JD032212

Key Points:

- Raindrop size distributions in Harvey and Florence were broadly similar to other tropical cyclones
- High concentrations of midsize drops were more common and widespread in Harvey than in Florence
- Harvey's rainfall was more intense and asymmetric due to vertical wind shear and a weaker intensity

Correspondence to:

J. C. DeHart,
jcdehart@colostate.edu

Citation:

DeHart, J. C., & Bell, M. M. (2020). A comparison of the polarimetric radar characteristics of heavy rainfall from Hurricanes Harvey (2017) and Florence (2018). *Journal of Geophysical Research: Atmospheres*, 125, e2019JD032212. <https://doi.org/10.1029/2019JD032212>

Received 7 DEC 2019

Accepted 26 APR 2020

Accepted article online 29 APR 2020

A Comparison of the Polarimetric Radar Characteristics of Heavy Rainfall From Hurricanes Harvey (2017) and Florence (2018)

Jennifer C. DeHart¹  and Michael M. Bell¹ 

¹Department of Atmospheric Science, Colorado State University, Fort Collins, CO, USA

Abstract Polarimetric coastal radar data are used to compare the rainfall characteristics of Hurricanes Harvey (2017) and Florence (2018). Intense rainfall was an infrequent yet important contributor to the total rainfall in Harvey, but its relative contribution varied spatially. The total rainfall over land maximized near the coast over Beaumont, TX, due to intense convection resulting from prolonged onshore flow downshear from the circulation center. Overall, polarimetric radar observations in Harvey show a dominance of high concentrations of small-to-medium drops, consistent with prior tropical cyclone studies. The microphysical characteristics were spatially and temporally inhomogeneous however, with larger drops more frequent on 27 August and higher number concentrations more frequent on 28 and 30 August. The polarimetric variables and raindrop characteristics observed during Florence share broad similarities to Harvey, but had reduced variability, fewer observations of stronger reflectivity and differential reflectivity, and a lower frequency of high number concentrations and medium-sized drops. The radar data indicate Florence had reduced coverage of stronger convection compared to Harvey. We hypothesize that differences in storm motion, intensity decay rates, and vertical wind shear produce the distinct precipitation structures and microphysical differences seen in Harvey and Florence.

1. Introduction

Heavy rainfall is a known hazard of tropical cyclones (TCs), responsible for 25% of hurricane fatalities in the United States (Rappaport, 2014). During the 2017 and 2018 Atlantic hurricane seasons, rainfall from Hurricanes Harvey and Florence set new state rainfall records in Texas and the Carolinas and caused destructive flooding. Over a 6-d period in August 2017, Hurricane Harvey stalled over coastal Texas and the peak rainfall observation of 1,538 mm near Nederland, TX, broke the continental and overall United States TC rainfall records previously held by Tropical Storm Amelia (1978) and Hurricane Hiki (1950), respectively. Equally noteworthy, rainfall exceeded 500 mm over a large area extending from southeast of Austin, TX, to the Texas-Louisiana border (Blake & Zelinsky, 2018). Just one year later, Hurricane Florence crept along the east coast of the United States, where accumulated rainfall totals of 912 mm over three days near Elizabethtown, NC, and 600 mm near Loris, SC, broke the TC precipitation records for each state. In each case, the extreme rainfall caused considerable impacts. Harvey caused over 65 direct deaths and widespread structural damage throughout southeast Texas (Blake & Zelinsky, 2018). In the Carolinas, Florence caused 22 direct fatalities, widespread flooding, and damage (Stewart & Berg, 2019).

Forecasting extreme rainfall is challenging since the accumulation results from intense rain rates, long duration events, or a combination of both factors. The microphysical processes that determine the surface rainfall intensity and drop size distribution (DSD) in a TC are a complex mixture of raindrop creation, growth, and melting ice (Black & Hallett, 1986, 1999; Houze et al., 1992; Marks & Houze, 1987). While the rotational storm dynamics and their interaction with the boundary layer are largely responsible for producing the vertical motion leading to precipitation, the environmental shear and the convective lifecycle also contribute to the strength and location of convective and stratiform precipitation in a TC (Chen et al., 2006; Corbosiero & Molinari, 2002; Didlake & Kumjian, 2017; Hence & Houze, 2011, 2012). Overall, the complicated interplay between microphysical processes and the kinematic and thermodynamic environments that determine their importance, all within a translating, rotating storm, make it a challenge to accurately predict the local rainfall accumulation.

In situ and surface microphysical observations from rain gauges and disdrometers provide important information about hydrometeor characteristics, but only represent a small region of a TC. Nonetheless,

disdrometer observations indicate that TC surface rainfall is typically dominated by numerous, midsize raindrops with median diameters of roughly 1–2 mm (Chang et al., 2009; Jorgensen & Willis, 1982; Tokay et al., 2008; Ulbrich & Lee, 2002; Wang et al., 2016). DSD characteristics can vary substantially in time and space and depend on the specific precipitation growth mechanisms. In Typhoon Haima (2004), convective rainfall periods were composed of numerous midsize drops with median diameters around 2 mm, whereas stratiform rainfall periods had fewer drops with smaller median diameters between 1.25 and 1.75 mm (Chang et al., 2009). However, the wind speed limitations of ground-based disdrometers restrict most studies to regions away from the eyewall (Chang et al., 2009; Tokay et al., 2008; Ulbrich & Lee, 2002; Wang et al., 2016).

Polarimetric radars can provide additional insight into the bulk hydrometeor shapes and concentrations over a much larger area (Bringi & Chandrasekar, 2001; Kumjian, 2013; Ryzhkov & Zrnic, 2019; Ryzhkov et al., 2005). Although operational polarimetric radars in the United States are relatively recent, their data have improved our understanding of TC microphysical processes. Brown et al. (2016) analyzed the rainfall characteristics from Hurricanes Arthur and Ana (2014) and found similar but distinct probability distributions of the DSDs in the two TCs that were in some cases substantially different than the DSDs produced by numerical simulations. Didlake and Kumjian (2017) also analyzed Hurricane Arthur (2014) and found that convection located in the downshear right quadrant of the TC produced columnar and planar crystals, which were advected downstream to the downshear left quadrant and fell as stratiform rain; despite different contributions from rain and ice processes, both quadrants exhibited heavy rain. The relative importance of rain and ice processes varies based on the precipitation feature and type.

Polarimetric analysis of the convective regions of a single rainband in Typhoon Matmo (2014) revealed a higher contribution of warm-rain processes to the surface rain, though ice processes were not insignificant (Wang et al., 2016). A case study of an outer rainband in Typhoon Nida (2016) showed more influence from convective ice processes (Wu et al., 2018). Case studies of Hurricanes Irene (2011) and Arthur (2014) revealed small ice was a weak contributor to the total ice water path in convective and stratiform precipitation, but was prevalent in low-reflectivity regions (Kalina et al., 2017). In addition to differences associated with specific features, processes can be influenced by environmental factors. Recently, Didlake and Kumjian (2018) and Feng and Bell (2019) found evidence of size sorting of raindrops in TCs due to the asymmetric vertical motion caused by the storm motion and deep layer vertical wind shear vector, respectively. The variety of conclusions with regard to the importance of different microphysical and dynamical processes in TCs underscore the spatial and temporal variability of rainfall production mechanisms as well as the variability in storm structure and environmental conditions.

Hurricanes Harvey and Florence offer an opportunity to study the bulk surface rainfall characteristics in two record-setting storms. Wolff et al. (2019) used polarimetric radar observations of Harvey to show that distinct DSD regimes impact rain rate retrievals and complicate the selection of parameters for attenuation-based algorithms. Through analyzing reanalysis and polarimetric radar data, Brauer et al. (2020) showed that strong horizontal moisture flux convergence, warm-rain processes, and rotating supercells all contributed to efficient precipitation processes in Harvey. Both Wolff et al. (2019) and Brauer et al. (2020) focused heavily on the precipitation processes and characteristics close to the Houston metropolitan area. In the current study, we focus on a broader region, including the rainfall maximum near Beaumont, TX, with the aim of better understanding the variability in rainfall in Harvey and the similarities and differences with rainfall in Florence.

The goal of this study is to characterize the nature of the extreme precipitation associated with Harvey and Florence, taking advantage of polarimetric radar data and the dense rain gauge network (where available). We approach this study through two perspectives: (1) assessing the relative contributions of intense and long-lasting rainfall and (2) examining characteristics of the near-surface rainfall inferred from polarimetric radar data. We first introduce our data processing methods (section 2). Then we decompose the surface precipitation from Harvey into intense and light rain, examine how the rainfall unfolded at two representative rain gauge locations, and use the polarimetric radar data from Harvey and Florence to compare the evolution and variability of the rainfall characteristics over a broad region of each storm (section 3). We then use the polarimetric radar data to derive metrics to describe the bulk DSDs in each storm (section 4). Finally, we propose hypotheses to explain the differences in the observed characteristics and the inferred microphysical processes from Harvey and Florence (section 5).

2. Data and Processing

2.1. Rain Gauge Data

Hourly precipitation data come from the Automated Surface Observing System (ASOS) network. Due to strong winds and heavy rainfall, many rain gauges failed during Harvey and Florence. We focus our analysis on the gauges that reported more than an average of 20 hourly observations per day. This requirement allows us to include stations that are missing an occasional hourly observation, while excluding stations that are missing too much data such that their statistics become meaningless. Most ASOS stations in Texas met the required number of hourly observations. Of the stations that did not meet the required number of hourly observations, all but one station failed for at least half the period, meaning the stations included were not sensitive to modest reductions in the required number of hours. The vast majority of stations failed during Florence, particularly in North Carolina, where only two ASOS stations met our hourly observations requirement. In South Carolina, roughly half the stations met our requirement and like Harvey, the stations that did not were also missing roughly half the observations. Unfortunately, the lack of adequate stations from Florence prevents a complete comparison between rain gauge data from Florence and Harvey.

2.2. Polarimetric Radar Data

The radar data used in this study come from the operational polarimetric Next Generation Weather Radar network. These radars have a wavelength of 10 cm (S band) and a 1° beamwidth, which allows for spatial resolution of order ~1 km over large distances with minimal attenuation. The key benefit of polarimetric capabilities is the inference of bulk hydrometeor characteristics through the use of both horizontally and vertically polarized radio waves (Bringi & Chandrasekar, 2001; Kumjian, 2013; Ryzhkov et al., 2005). In Rayleigh scattering regimes, the radar reflectivity at horizontal polarization Z_H is proportional to the power returned from the backscatter due to both raindrop size and concentration, although it is more sensitive to the former due to the dependence on the sixth power of the drop diameter. The differential reflectivity Z_{DR} is defined as the difference between the reflectivity at horizontal and vertical polarization and is proportional to the median drop size of the DSD. The correlation coefficient ρ_{HV} is defined as the correlation of the horizontal and vertical pulses, with high values associated with nearly spherical targets like raindrops, and lower values typically associated with biological targets or mixed phase conditions within the pulse volume. The specific differential phase K_{DP} is the local change in the difference between the vertical and horizontal phase shifts and is proportional to the liquid water content, which depends on both the drop size and number concentration.

Located just west of Galveston Bay, the Houston radar (KHGX) captured the vast majority of Harvey's precipitation. Along the coast in central North Carolina, the Morehead City radar (KMHX) was situated to the northeast of Florence's maximum precipitation, but unfortunately went offline after 1800 UTC on 15 September, missing the final 24 hours of rainfall. While the nearby Wilmington radar (KLTX) was better positioned than KMHX and operated over a longer period, it suffered from an apparent Z_{DR} bias and intermittent dropouts (not shown). Although applying an estimated bias correction to the KLTX data produced results that were reasonably consistent with the KMHX radar, we focus our analysis on the higher-quality KMHX data to provide a better comparison with the high-quality radar data from Harvey.

To ensure the best representation of near-surface characteristics, we restrict the majority of our analysis to data from the lowest elevation angle (0.5°) from each radar. We retain the native polar coordinates of the radar to avoid interpolation, but the total and fractional coverage of each polarimetric variable and derived metric category at each range gate are weighted by the distance from the radar to account for beam spreading at larger radii. We exclude data beyond 127 km from the radar to limit contamination by ice above the melting layer. We note that by including all data within 127 km of KHGX our analysis encompasses a larger area than the one used by Wolff et al. (2019), which focused on the region immediately surrounding the Harris County Flood Warning System Network.

LROSE software (Bell, 2019) was first used to determine the most likely hydrometeor type according to the National Center for Atmospheric Research (NCAR) Particle ID (PID) fuzzy logic algorithm (Vivekanandan et al., 1999). We then isolated all radar pixels that were classified as light, moderate, or heavy rain and also had ρ_{HV} values between 0.95 and 1.0, inclusive, to retain only rain in our analysis. We performed an additional subjective quality control by identifying persistent signals of reduced or elevated Z_{DR} along entire beams and removed those beams from the analysis. This processing resulted in the removal of 20 beams

(2.8%) from KHGX believed to have been compromised by partial beam blockage, while no beams from KMHX were compromised.

K_{DP} estimation in LROSE is based on an updated version of the Hubbert and Bringi (1995) method. First, ϕ_{DP} is unfolded to create a monotonically increasing field. The unfolded ϕ_{DP} field is smoothed using a finite impulse response filter, similar to Hubbert and Bringi (1995), except using fewer iterations. Local bumps in the smoothed ϕ_{DP} field due to backscatter differential phase (δ) are removed before another finite impulse response filter is applied for additional smoothing. Finally, the algorithm computes K_{DP} as the derivative of the smoothed and corrected ϕ_{DP} . While K_{DP} can be negative in ice regions, negative values are unphysical in rain and indicative of noise in the derivative calculation. To further reduce the impact of noise on our analysis, we removed all radar gates where K_{DP} was negative.

The Cunningham et al. (2013) technique was used to estimate Z_{DR} bias due to calibration errors by applying the technique to low-reflectivity regions in each radar sweep and averaging together the individual biases over all sweeps where the number of samples surpassed 500. With this technique, we calculated Z_{DR} bias corrections of -0.25 and -0.07 dB to KHGX and KMHX, respectively. At times, we also noticed odd jumps in the mean Z_{DR} at KHGX, which were well outside the mean bias correction and we deemed to be unphysical. We removed 22 of the 0.5° sweeps that exhibited strong jumps in the mean Z_{DR} compared to the surrounding times.

2.3. Storm and Shear Data

The storm intensity and location data for Harvey and Florence come from the National Hurricane Center Best Track dataset. The deep-layer wind shear magnitude and direction for Harvey come from the Statistical Hurricane Intensity Prediction Scheme database (DeMaria et al., 2005). Since the final predictors had not been released for 2018 at the time of this manuscript, we use the real-time Statistical Hurricane Intensity Prediction Scheme predictors for Florence. In each case, the deep-layer shear is calculated from 850–200 hPa over radii between 0 and 500 km from the storm center after the vortex has been removed.

3. Rain Gauge and Polarimetric Radar Characteristics

3.1. Harvey Rainfall

Harvey first made landfall near Rockport, TX as a Category 4 hurricane (Blake & Zelinsky, 2018). Weak steering flow slowed and eventually reversed the inland movement, sending Harvey back to the Gulf of Mexico around 1200 UTC on 28 August. Although the *center* of Harvey remained at least 170 km from Houston, heavy rain accumulated near Houston and Beaumont between 0000 UTC on 25 August and 0000 UTC on 31 August as persistent onshore flow rose over a stationary front (Blake & Zelinsky, 2018). Overall, rain gauges near the coast measured the largest rainfall accumulations (Figure 1a). Notably, Houston's George Bush Intercontinental Airport (KIAH) and Beaumont's Jack Brooks Regional Airport (KBPT) received 794 and 1,207 mm in five days, respectively.

Event totals alone are insufficient for understanding extreme rainfall, which depends on both rain rate and event duration. Given Harvey's slow motion, it is clear that the long period of rainfall was an important factor. In an attempt to untangle the two effects, we isolate the frequency and fractional contribution of intense rain, which we define as a rain rate exceeding 25.4 mm hr^{-1} (1 in hr^{-1}). This threshold is consistent with the minimum rain rate of 25 mm hr^{-1} used by Hitchens et al. (2013) to define heavy rain in their climatology of hourly rain rates in the continental United States. Hitchens et al. (2013) show that such a rain rate is infrequent but not rare. Gauge-adjusted radar estimates of precipitation suggest 10^6 instances of 25 mm hr^{-1} rain rates and $10^2\text{--}10^3$ instances of 150 mm hr^{-1} rain rates occur each year, compared to over 10^7 instances of 10 mm hr^{-1} rain rates (Hitchens et al., 2013). For each station, we calculate the frequency of intense and light rain (excluding hours with no rain) and their relative contributions to the total storm rainfall over the five-d period. By our definition, intense rain was infrequent and comprised no more than one fourth of all raining hours, but the intense rain occurrence was closely associated with the total rain (Figure 1). Intense rain contributed nearly one third of the total rain in the Houston metro area. Meanwhile, intense rainfall made up one fourth of all hours with measurable rainfall at stations close to the Louisiana border and was responsible for nearly two thirds of the total rain. The two stations near Beaumont, TX, consistently saw a larger fraction of the total rainfall come from intense rain rates than all but one station, regardless of whether intense rainfall threshold was 20 , 30 , 40 , or 50 mm hr^{-1} (not shown). The only other

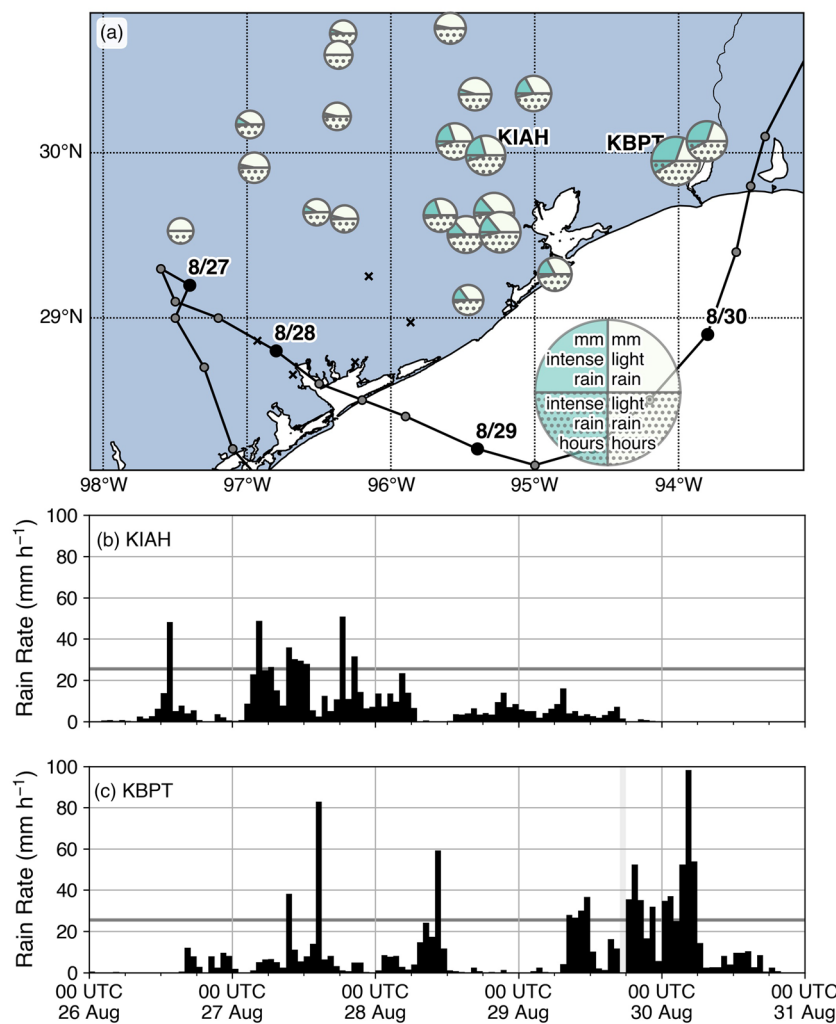


Figure 1. (a) Map of Hurricane Harvey rainfall from 0000 UTC on 25 August to 0000 UTC on 31 August 2017. Circle size is proportional to the square root of the total rainfall, to limit the overlap of station plots. Within each circle, the lower semicircle (hashed) displays the frequencies and the upper semicircle (solid) displays the contribution to the total rainfall by intense (green) and light (white) rainfall. Only hours with measurable rainfall are included. Locations marked by an “x” indicate rain gauges missing more than an average of four observations per day. (b) Hourly rainfall time series at KIAH. (c) Hourly rainfall time series at KBPT. Black horizontal line indicates an hourly rain rate of 25 mm hr⁻¹, which is used to identify intense rain. Vertical gray bars indicate missing data.

station that had comparable fractional contribution of intense rainfall when the intense rainfall threshold was 40 or 50 mm hr⁻¹ is located on the west side of Houston (29.62°N, -95.65°W). The gauge observed less rainfall than the Beaumont gauges and most of the Houston gauges and three hours of intense rain were able to make a larger fractional contribution. Both intense rain rates and the long duration were important, but their relative importance varied across Texas.

The spatial variability of rainfall evolution is highlighted in the precipitation time series for KIAH and KBPT (Figures 1b and 1c). We focus on the 120-hr (5-d) period after 0000 UTC on 26 August as it encompasses most of the rain at each location (KIAH: 99%; KBPT: 97%). Overall, the hourly KIAH time series is consistent with the 15-minute observations from the Harris County Flood Warning System gauges (Wolff et al., 2019). To first order, Harvey’s slow eastward movement dominates differences between the time series in Houston and Beaumont. The daily rainfall at KIAH peaked on 27 August as the center of Harvey passed by Victoria, TX, placing the Houston metro area closer to the circulation center and directly in the onshore flow. Meanwhile, rainfall at KBPT peaked during the 12-hr period surrounding 0000 UTC on 30 August as the center of Harvey moved southeast of Houston, when Beaumont was closer to the storm center. At both airports, the peak

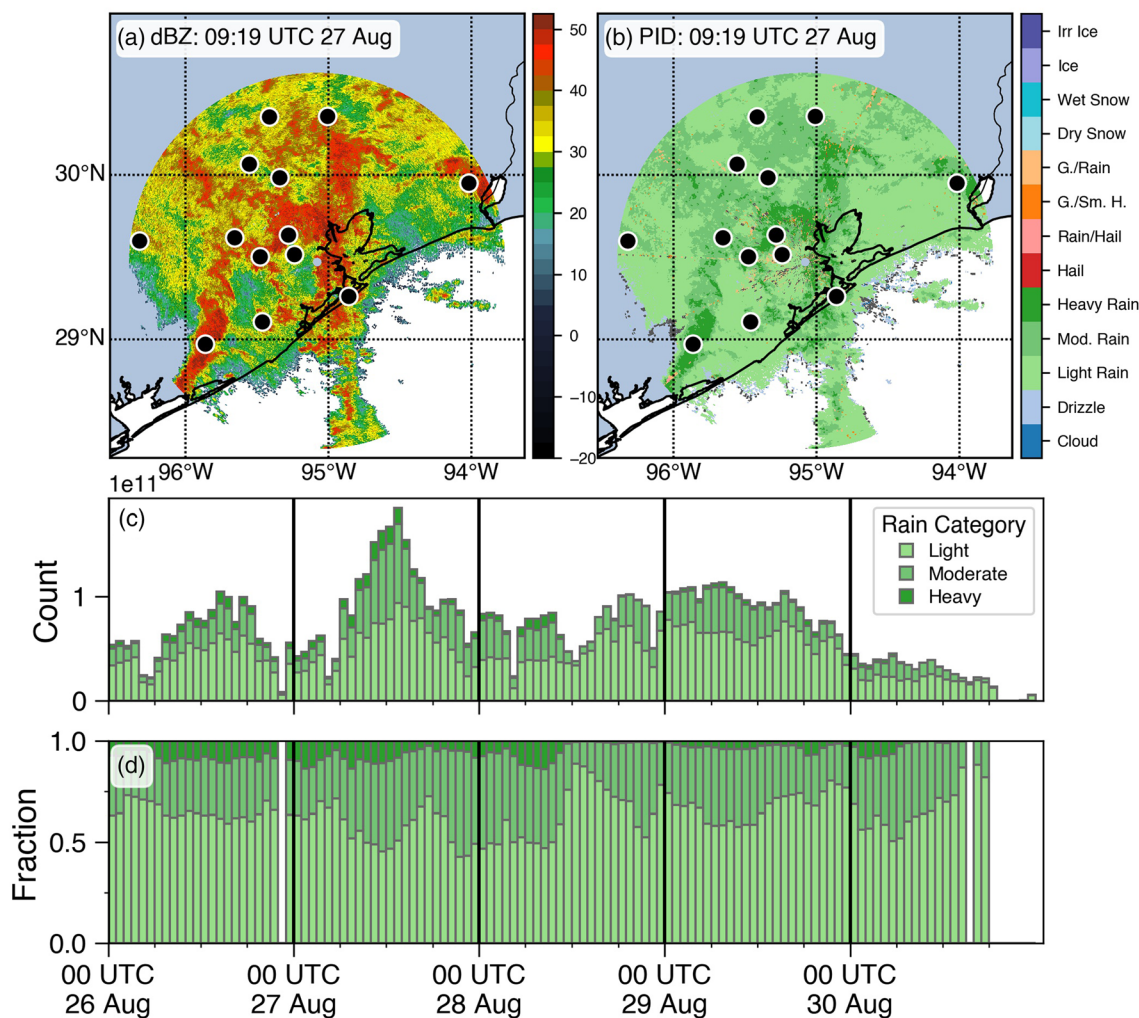


Figure 2. (a) Map of reflectivity from the 0.5° plan position indicator (PPI) scan from KHGX at 0919 UTC on 27 August 2017. Only data within 127 km of KHGX are displayed. The black circles represent the location of ASOS rain gauges within 127 km of KHGX. (b) As in (a), but for the PID categories. (c) Hourly time series of range-weighted counts of rain PID categories. (d) As in (c), but for the range-weighted fraction.

rainfall was strong and steady, but rain rates were more intense at KBPT. Before the peak rainfall, both locations observed intermittent intense rain suggesting embedded convection within a broader region of stratiform precipitation. KBPT was in this regime for a longer period than KIAH and only light rain occurred at KIAH after Harvey pushed east. The period of light rain should not be disregarded, as it amounts to 20% of the total precipitation at KIAH. But the combination of prolonged convection and more intense rain rates led to more precipitation at KBPT than KIAH.

3.2. Polarimetric Characteristics of Harvey

As discussed in the introduction, a key benefit of polarimetric radars is the ability to infer microphysical characteristics over a large area. A sample sweep from the KHGX radar shows widespread rain over southeast TX on 27 August (Figure 2a). Radar reflectivity values above 40 dBZ are frequent, but the echo intensities are not uniform and the NCAR PID algorithm identifies differences in the rain intensity (Figure 2b). To examine the radar data through time, we select all radar gates classified by the PID as light, moderate, or heavy rain. In Vivekanandan et al. (1999), these categories roughly correspond to rain rates of <10 , <40 , and $>40 \text{ mm hr}^{-1}$, respectively. These categories do not match our definitions of light and intense rainfall, since our primary usage of the PID categories is merely to identify likely raining radar echoes. Some infrequent echoes believed to be falsely identified as graupel are excluded from our analysis (Figure 2b).

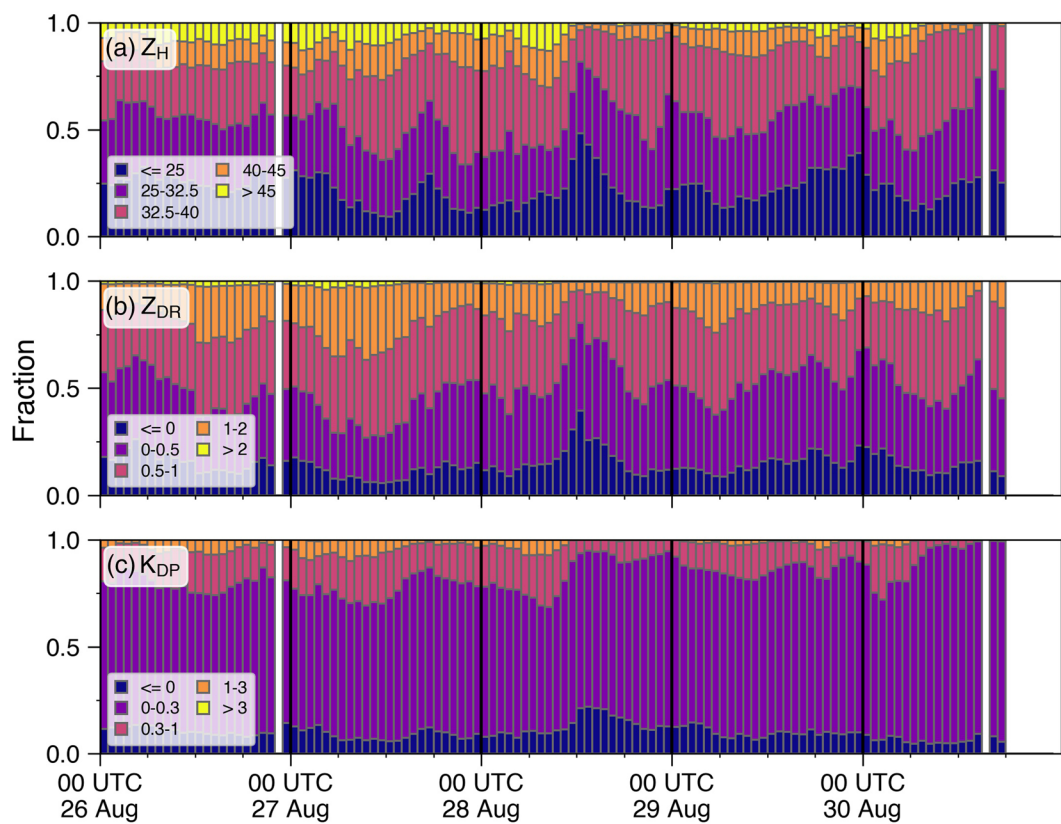


Figure 3. Hourly time series of range-weighted fraction of polarimetric variables in specified bins at KHGX of (a) reflectivity (dBZ), (b) differential reflectivity (dB), and (c) specific differential phase ($^{\circ}$ km $^{-1}$).

Once the raining areas are identified, we count the frequency of each PID rain category within 127 km of the radar. We weight the count for each radar gate by its distance from the radar to account for beam spreading at larger range distances and aggregate the weighted counts at each hour to create a time series of hourly PID counts (Figure 2c). We include data over the ocean, but our results are not sensitive to the exclusion of offshore data points. Rain was widespread and peaked in coverage on 27 August. Harvey's exit from the radar domain is visible in the diminishing counts after 1200 UTC on 30 August. Occasional missing or bad radar sweeps yield gaps in the time series. To determine the relative importance of each PID category for each hour over the precipitating area, we examine the fractional coverage of the PID categories (Figure 2d). Any periods when the weighted count failed to exceed 2×10^{10} were removed to ensure a sufficient sample size. Overall, light rain was the dominant PID category, but heavy and moderate rains were more frequent before 1200 UTC on 28 August. A slight resurgence in moderate rain occurred between 0000–0600 UTC on 30 August.

Using these rain categories to identify likely precipitating echo, we examine the distributions of Z_H , Z_{DR} , and K_{DP} to determine the dominant microphysical characteristics. One prominent feature of the distributions is the modest values of each polarimetric variable, consistent with a midsize-drop dominated regime (Figure 3). Z_H and Z_{DR} values lie mostly below 45 dBZ and 2 dB, respectively, consistent with prior studies (Brown et al., 2016; Wang et al., 2016; Wolff et al., 2019, and Brauer et al., 2020). K_{DP} values infrequently surpass the 0.3° km $^{-1}$ threshold often used for K_{DP} -based rain rate algorithms, similar to K_{DP} values estimated from disdrometer observations in tropical convection over the Indo-Pacific warm pool (Thompson et al., 2018). Despite modest values overall, Z_H , Z_{DR} , and K_{DP} values were larger in the first half of the event, consistent with the increased prevalence of moderate and heavy rain identified by the PID algorithm. The K_{DP} values in our analysis cover the same range as the values obtained by Wolff et al. (2019), but our distribution skews toward weaker values. Our area of analysis is roughly a factor of 4 larger than Wolff et al. (2019) that focused on a rectangle located in the northwest quadrant of the radar domain to compare radar-estimated

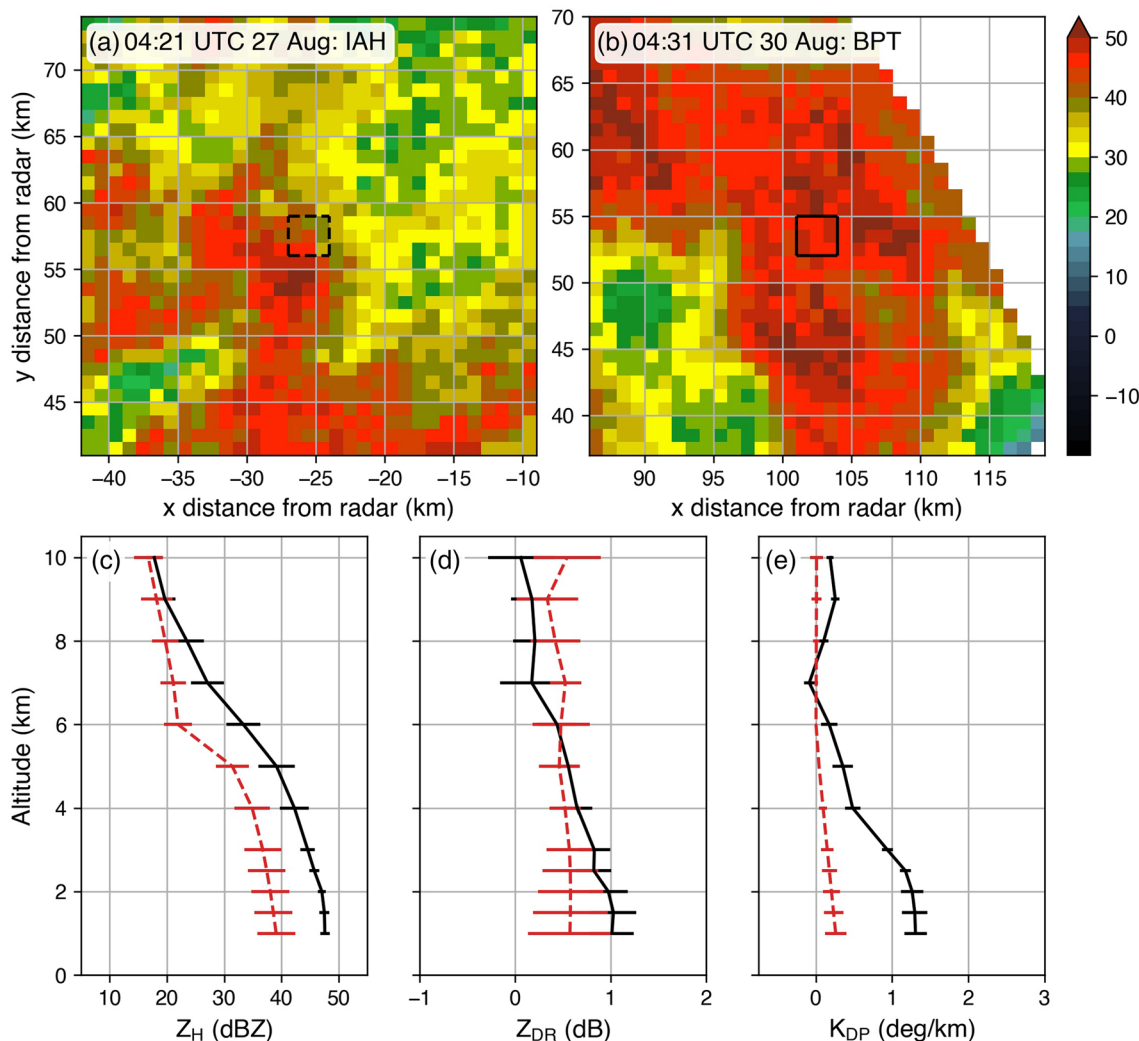


Figure 4. (a) Map of gridded radar reflectivity data at 1-km altitude within a 32×32 -km box surrounding KIAH at 0421 UTC on 27 August 2017 during Hurricane Harvey. Black dashed box indicates the area over which the vertical profiles are calculated. (b) As in (a), but for KBPT at 0431 UTC on 30 August 2017. Black solid box indicates the area over which the vertical profiles are calculated. (c) Vertical profiles of Z_H near KIAH (dashed red line) and KBPT (solid black line). Error bars denote the standard deviation at each altitude. (d) As in (c), but for Z_{DR} . (e) As in (c), but for K_{DP} .

rain rates with rain gauges in the Harris County Flood Warning System Network. We also use a slightly different algorithm to estimate K_{DP} . Since the estimated K_{DP} values span a similar range of values, we hypothesize that the different regions of analysis contribute the most to the difference in K_{DP} values.

The greatest shift to larger reflectivity values in the full-domain distributions occurred in two periods: 0600 UTC on 27 August through 1200 UTC on 28 August and 0000–0600 UTC on 30 August (Figure 3a). Despite similar reflectivity distributions, Z_{DR} values were greater in between 0300 and 0900 UTC 27 August, indicating larger drops were responsible for the higher reflectivities (Figure 3b). The simultaneous increase in Z_H and Z_{DR} values on 27 August were noted by both Wolff et al. (2019) and Brauer et al. (2020). Although the larger-domain hourly time series show that the most intense values only persisted for half the day. In contrast to the high Z_{DR} values on 27 August, the high reflectivities on 30 August coincided with reduced Z_{DR} values, indicative of smaller drops. In between was a 36-h period (1200 UTC on 28 August to 0000 UTC 30 August) of weak reflectivity values across the domain. The coincident decrease in Z_{DR} and K_{DP} values around 1200 UTC 28 August suggests a decrease in the drop size. There was a similar weakening of the polarimetric variables after the second heavy rain peak (\sim 1200 UTC 30 August), but the echo coverage at this time was minimal (Figure 2c).

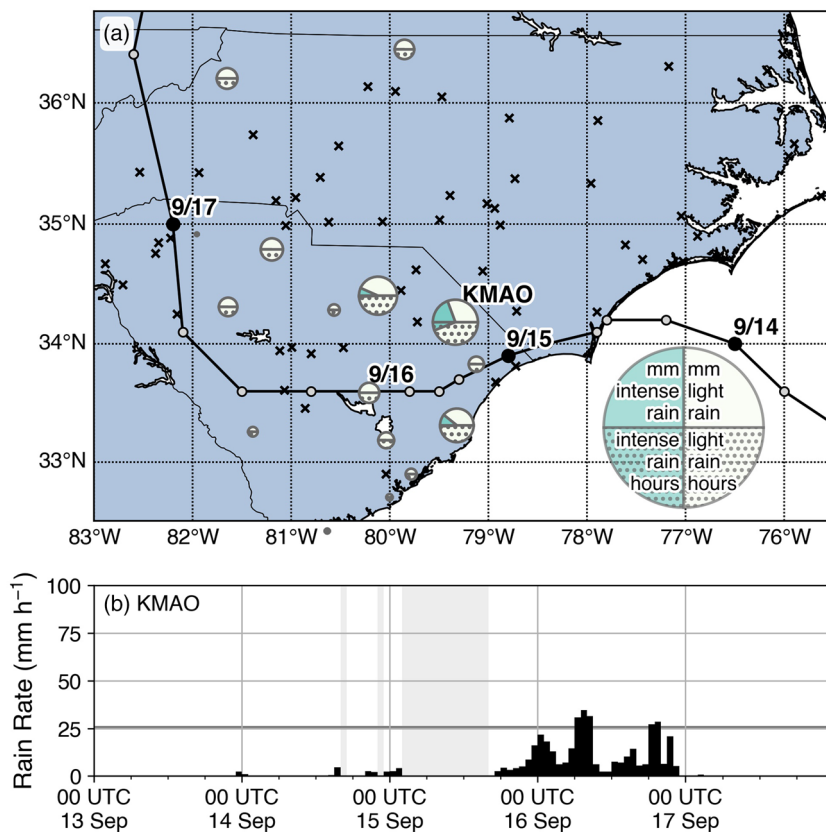


Figure 5. (a) As in Figure 1, but of Hurricane Florence rainfall from 0000 UTC on 13 September to 0000 UTC on 18 September 2018. (b) Hourly rainfall time series at KMAO. Black horizontal line indicates an hourly rain rate of 25 mm hr^{-1} , which is used to identify intense rain. Vertical gray bars indicate missing data.

To get a sense of how the polarimetric data relate to the rain gauge data at key time periods, we compare radar data surrounding KIAH and KBPT during hours when the stations experienced their heaviest rainfall. Figure 4 shows snapshots of gridded radar data near KIAH and KBPT during those hours of intense rainfall. Radar data were gridded with LROSE Radx2Grid software with horizontal grid spacing of 1 km and vertical grid spacing of 0.5 km below 3-km altitude and 1.0 km above 3-km altitude. Near KIAH, the 0421 UTC radar observation on 27 August coincided with an hourly rain gauge observation of nearly 50 mm. Reflectivity values at 1-km altitude within 32 km of the gauge ranged from 25–50 dBZ, while those immediately next to the gauge exhibited a narrower range between 35 and 45 dBZ (Figure 4a). Meanwhile, near KBPT, the 0431 UTC radar observation on 30 August coincided with an hourly rain gauge observation of almost 100 mm, which was the highest rain rate at that location. Although 1-km altitude reflectivity values surrounding the gauge spanned a similar range as observed near KIAH days prior, reflectivity values were more homogeneous, with a large area of reflectivity values exceeding 40 dBZ (Figure 4b). Comparing the vertical profiles of Z_H , Z_{DR} , and K_{DP} shows that each variable was generally more intense near KBPT throughout the atmosphere, with the exception of Z_{DR} values above 6-km altitude, where the spread was large (Figures 4c–4e). All three polarimetric profiles increase toward the surface near KBPT, consistent with enhanced collision-coalescence processes (Kumjian & Prat, 2014). Meanwhile, Z_H increases toward the surface near KIAH, but the K_{DP} increase toward the surface is weaker and Z_{DR} exhibits a lot of spread, including both positive and negative slopes. The variability in vertical structure is not surprising given the heterogeneous low-level reflectivity field near KIAH at this time; Brauer et al. (2020) also showed that vertical polarimetric profiles over nearby downtown Houston varied substantially on 27 August.

3.3. Florence Rainfall

The outer rainbands of Florence approached North Carolina on 13 September and Florence made landfall in southeast North Carolina on 14 September as a Category 1 storm. Similar to Harvey, forward motion slowed as Florence crept slowly into South Carolina before accelerating northward late on 16 September

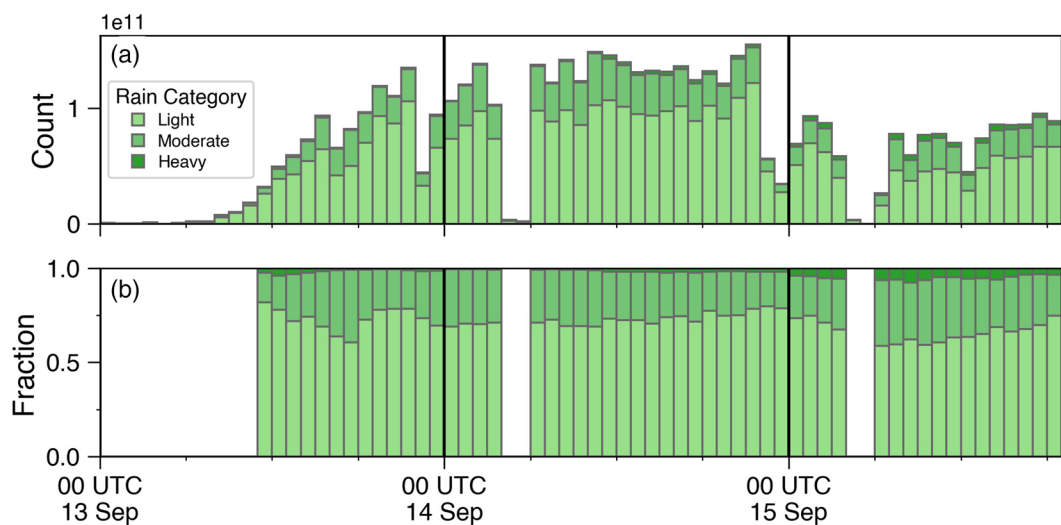


Figure 6. Hourly time series of range-weighted PID categories from KMHX by (a) total count and (b) fraction.

(Figure 5). Unfortunately, extensive rain gauge outages in the region of maximum rainfall preclude a breakdown of rain rates for Florence, as indicated by the number of stations with too many hours of missing data in Figure 5. The available data reveal two big differences from Harvey, however. First, Florence was a shorter event as most gauges observed rainfall for approximately three days. Second, the available rain rates from Florence are comparable, yet slightly weaker than the rain rates in Figures 1b and 1c, although rain rates likely strengthened on 15 September when most gauges were offline. As discussed in section 2, the Morehead City, NC, radar (KMHX) also went offline midway through the event (~1800 UTC 15 September), missing the final 12–24 hours of rainfall over North Carolina. Despite missing data, we think the high radar data quality, sufficient length of the data record (> 48 h), and similar statistics to bias-corrected KLTX radar data allow for a reasonable comparison of Florence's rainfall characteristics derived from KMHX and the rainfall characteristics from Harvey.

3.4. Polarimetric Characteristics of Florence

Similar to Harvey, polarimetric data from Florence are dominated spatially and temporally by the light rain PID category (Figure 6a). The magnitude of range-weighted counts is similar, although KMHX observed more offshore pixels than KHGX. Similar to Harvey, our results are not sensitive to the exclusion of offshore data points. The range-weighted counts increased slowly on 13 September as Florence approached the east coast, before plateauing on 14 September (Figure 6b). As Florence moved southwest away from the radar, the range-weighted counts decreased on 15 September. At the same time, the fractional coverage of moderate and heavy rain categories increased (Figure 6c).

The polarimetric distributions exhibit similar TC characteristics to Harvey, although most values are generally lower. Reflectivity values seldom exceed 45 dBZ, differential reflectivity values never exceed 2 dB, and K_{DP} values are lower than those seen during Harvey (Figure 7). The lower polarimetric values are consistent with the values observed in an inner rainband in Wu et al. (2018). Greater coverage of the moderate intensity values corresponds to reduced coverage of heavier rain rates in comparison to Harvey. Additionally, the polarimetric distributions from Florence gradually shift to higher values after 0600 UTC on 15 September in contrast to the more episodic nature of Harvey's variability. The increase in coverage of Z_H , Z_{DR} , and K_{DP} above 40 dBZ, 1 dB, and $0.3^\circ \text{ km}^{-1}$, respectively, are the closest the polarimetric values from Florence approach the statistics from the first 60 hours of Harvey (Figure 3). Even if these statistics persisted for the final 24 hours that Florence impacted North Carolina, the length of influence by heavier rain rates would only amount to 48 hours. The amount of intense polarimetric values in Florence was reduced spatially and temporally in comparison to Harvey.

Although most rain gauges failed in Florence, we can still examine representative vertical profiles of polarimetric quantities. Due to the lack of suitable rain gauge comparisons, we chose instead to highlight the vertical structure of two different TC features: a convective outer rainband and an inner rainband. Figure 8

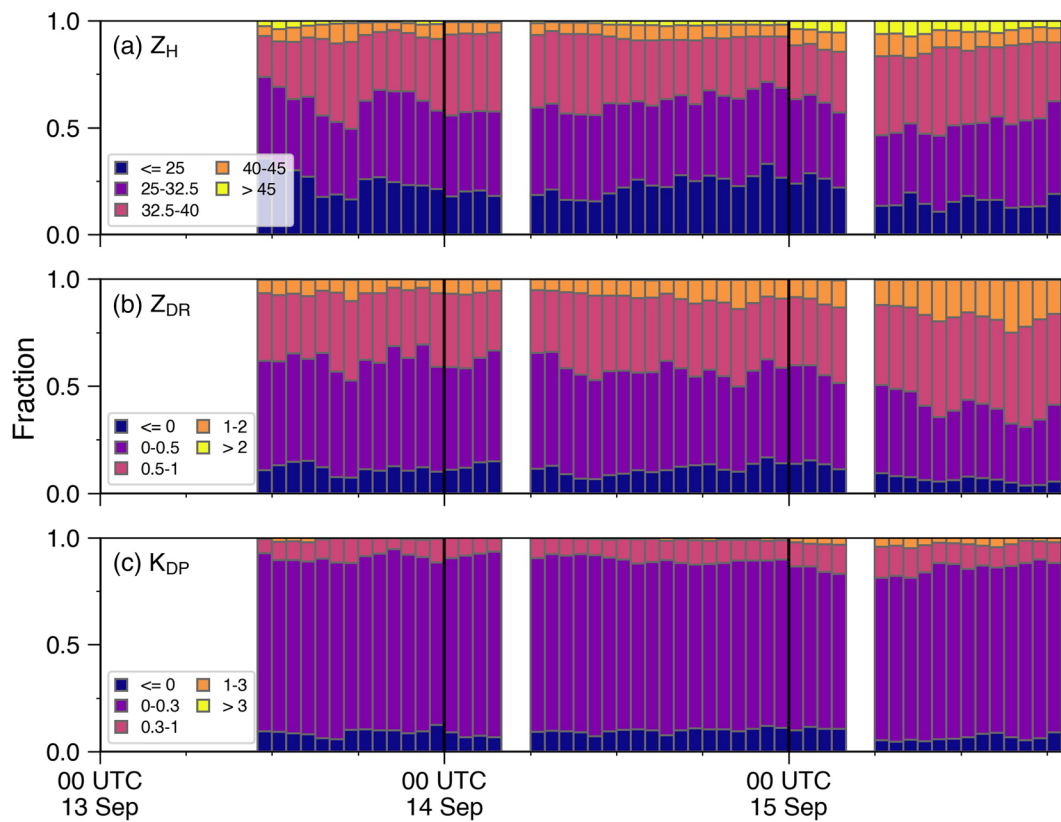


Figure 7. As in Figure 3, but for data from KMHX.

shows snapshots of the horizontal and vertical structure of two rainbands occurring simultaneously in Florence on 14 September 2018. The outer rainband exhibits a similar structure as the examples from Harvey in Figure 4, with heterogeneous horizontal patterns of reflectivity at 1 km and reflectivity peaking between 45 and 52 dBZ. The vertical profiles of the polarimetric variables in the outer rainband shown in Figures 8c–8e are similar to those near KBPT during Harvey on 30 August, where Z_H , Z_{DR} , and K_{DP} all increase toward the ground as collision-coalescence processes are enhanced (Kumjian & Prat, 2014). Meanwhile, the inner rainband shows more modest increases in Z_H and K_{DP} near the surface, and the Z_{DR} profile varies little below 4 km. These localized profiles combined with the examples from Harvey underscore the variety of microphysical processes that can exist in a TC, consistent with prior studies (Didlake & Kumjian, 2018; Wang et al., 2016; Wu et al., 2018). A more systematic examination of the vertical polarimetric profiles with respect to both TC features and surface rainfall is beyond the scope of this study but is recommended for future work.

4. Estimated DSD Characteristics

To better understand the covariability of the raindrop size and number concentration, we retrieve specific metrics related to the DSD from the radar data. A DSD can be approximated as a gamma distribution with the following form:

$$N(D) = N_0 D^\mu \exp(-\Lambda D) \quad (1)$$

where N_0 is the intercept parameter, D is the drop diameter, μ is the shape parameter, and Λ is the slope parameter (Ulbrich, 1983). The distribution can be normalized (Willis, 1984) to compare different DSDs using a modified intercept parameter proportional to the liquid water content and median drop diameter:

$$N_W = \frac{1.81 \times 10^5 LWC}{\pi \rho_L D_0^4} \quad (2)$$

where N_W ($\text{m}^{-3} \text{ mm}^{-1}$) is the normalized intercept parameter, LWC (g m^{-3}) is the liquid water content, ρ_L (g cm^{-3}) is the density of liquid water, and D_0 (mm) is the median volume diameter. N_W and D_0 can

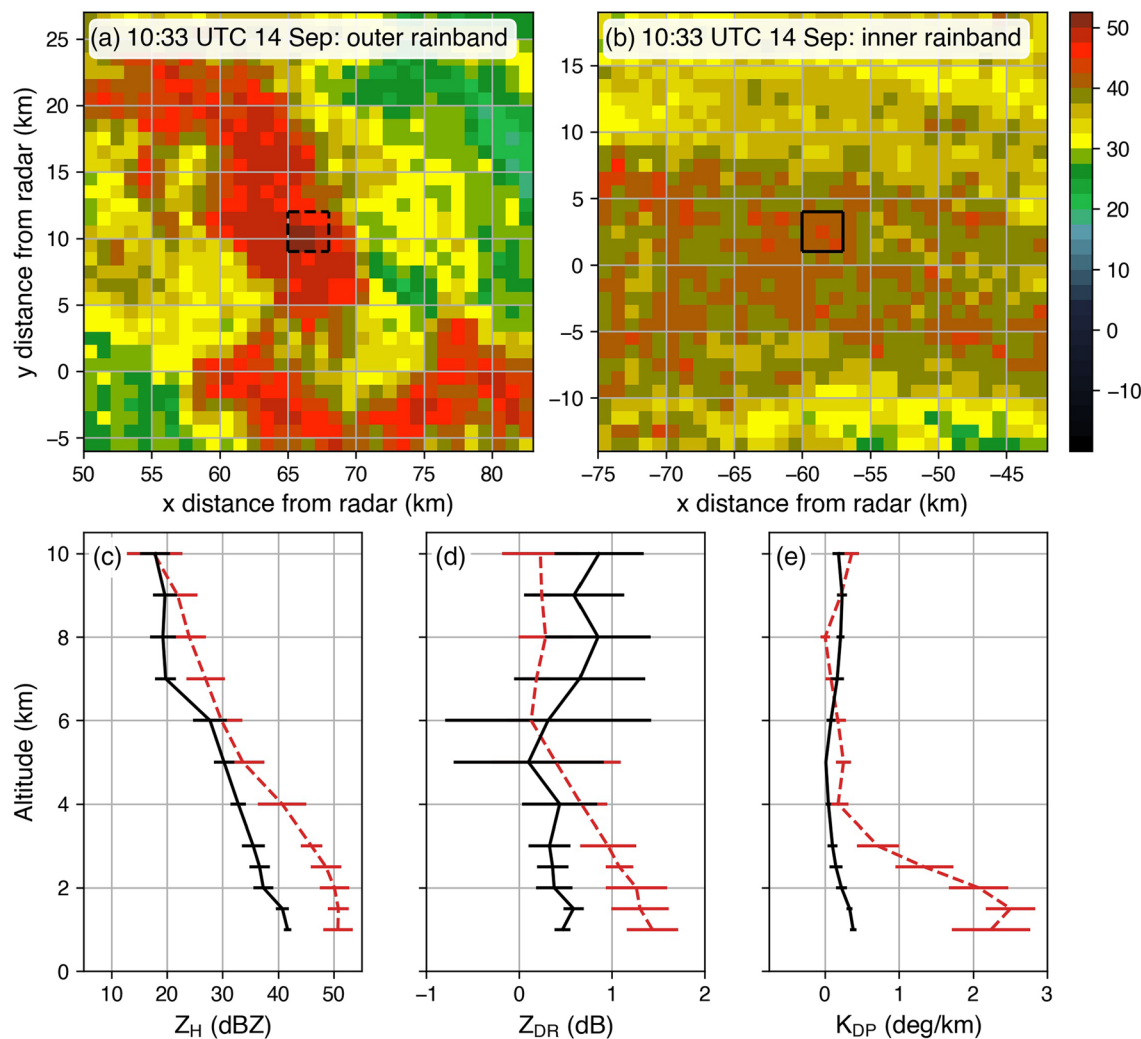


Figure 8. (a) Map of gridded radar reflectivity data at 1-km altitude within a 32 × 32-km box surrounding an outer rainband at 1033 UTC on 14 September 2018 during Hurricane Florence. Black dashed box indicates the area over which the vertical profiles are calculated. (b) As in (a), but surrounding an inner rainband. Black solid box indicates the area over which the vertical profiles are calculated. (c) Vertical profiles of Z_H near the outer rainband (dashed red line) and inner rainband (solid black line). Error bars denote the standard deviation at each altitude. (d) As in (c), but for Z_{DR} . (e) As in (c), but for K_{DP} .

be considered proxies for the number of drops and the median drop size. Although an assumed gamma distribution cannot represent all observed DSDs, gamma distributions are prevalent within the literature and are an effective way of identifying meaningful spatial and temporal changes in the type of DSD (Bringi et al., 2003; Chang et al., 2009; Thompson et al., 2015; Wang et al., 2016; Willis, 1984; Zagrodnik et al., 2018). Without disdrometer measurements of D_0 and N_W , we use the CSU RadarTools package (Lang et al., 2019) to estimate these parameters from polarimetric data following the algorithm described by Bringi et al. (2015) where D_0 and N_W are related to Z_{DR} and Z_H through the following equations:

$$D_0 = \begin{cases} 0.0536Z_{DR}^3 - 0.1971Z_{DR}^2 + 0.6261Z_{DR} + 1.0815, & Z_{DR} \geq 1\text{dB} \\ 0.0424Z_{DR}^4 - 0.4571Z_{DR}^3 + 0.6215Z_{DR}^2 + 0.457Z_{DR} + 0.8808, & Z_{DR} < 1\text{dB} \end{cases} \quad (3)$$

$$N_W = 19.76 \frac{Z_H}{D_0^{7.46}} \quad (4)$$

We exclude data where Z_{DR} is below −0.5 dB, though such data points are infrequent. To understand how the DSDs are broadly related to water content, we obtain a theoretical estimate of LWC by rearranging equation (2). Infrequent big drop and numerous small drop DSDs can produce similar LWC values, despite

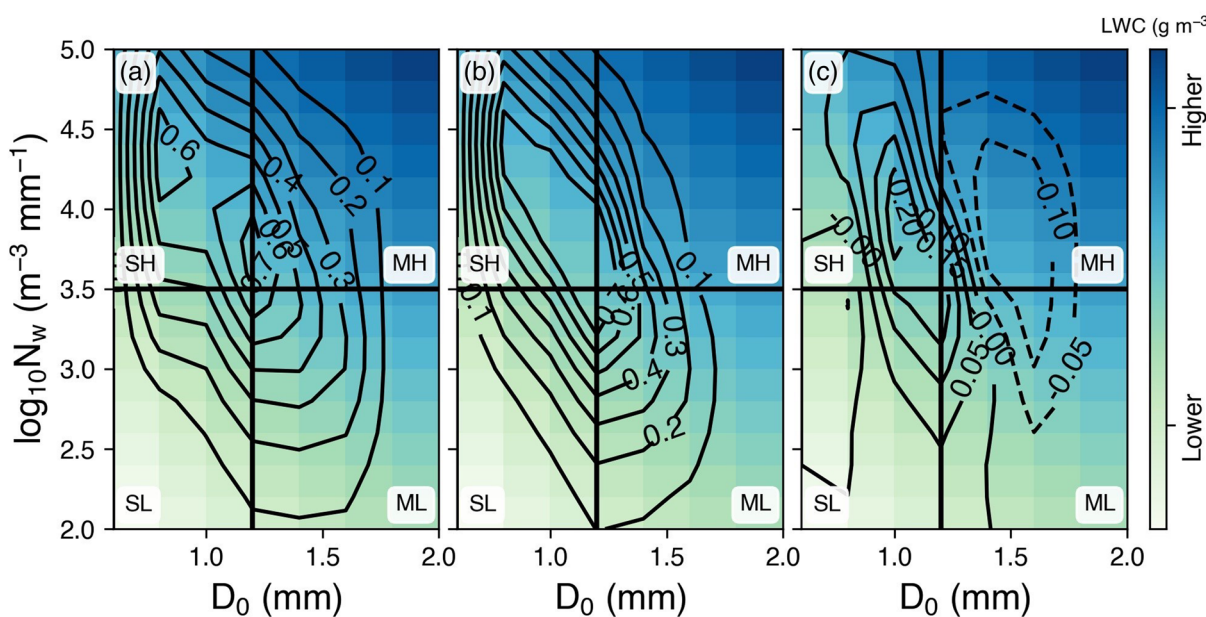


Figure 9. (a) Joint probability distribution (contours) of range-weighted N_w and D_0 values calculated from the KHGX polarimetric data for Harvey between 0000 UTC on 26 August and 0000 UTC on 31 August. Theoretical LWC values (colors) are calculated from equation (2). Labels indicate the different DSD quadrants (SL: low-concentration small drops, ML: low-concentration medium drops, SH: high-concentration small drops, and MH: high-concentration medium drops). (b) As in (a), but for data from KMHX for Florence between 0000 UTC on 13 September and 1922 UTC on 15 September, when the radar went offline. (c) The difference joint probability distribution between Florence/KMHX and Harvey/KHGK (dashed contours indicate frequencies were greater for KHGK).

distinct radar signatures and formation processes (Figure 9). As discussed by Chang et al. (2009), precipitation radar estimates such as those from S band can miss the numerous ($\log_{10}(N_w) > 4$), small drop ($D_0 < 1$ mm) DSDs due to limitations in radar sensitivity, which can cause an underestimate of the LWC from precipitation radar estimates. Despite these uncertainties, by using the same algorithm and radar wavelength to estimate N_w and D_0 in Harvey and Florence, we can quantitatively compare the drop size characteristics of the two TCs, while qualitatively comparing with previous studies that use disdrometer measurements or different radar retrieval techniques.

Figure 9a shows that numerous small drop DSDs were common in Harvey, which is broadly consistent with previous studies on TC DSDs (Chang et al., 2009; Tokay et al., 2008; Wolff et al., 2019). The retrieval suggests Harvey's dominant DSD type lies in between small drop DSDs from maritime convection (Bringi et al., 2003; Thompson et al., 2015) and large drop DSDs that can occur in continental, wintertime precipitation (Zagrodnik et al., 2018), but the spread differs from other polarimetric estimates of DSD parameters in TCs. The retrieved DSDs exhibit lower concentrations than Wang et al. (2016) by an order of magnitude ($\Delta 1$ in $\log_{10}(N_w)$ space) and the median drop diameters are approximately 0.5 mm smaller than the values retrieved by Chang et al. (2009). That being said, we emphasize that these two studies use a different technique (Zhang et al., 2001) that estimates N_0 and Λ in equation 1 rather than the parameters estimated here in equation (2). To test the sensitivity to the retrieval algorithm, we calculated the DSD parameters using the relationship obtained by Brandes et al. (2004). The resulting N_w - D_0 distributions, the temporal evolution of each storm, and the differences between Harvey and Florence were quite similar using either the Bringi et al. (2015) or Brandes et al. (2004) retrievals (not shown). As a result, we feel confident that our comparisons between Harvey and Florence using the same retrieval technique reveal differences in rainfall characteristics and microphysical processes between the two storms. Further comparisons with other storms may reflect retrieval technique uncertainty in addition to differences in microphysical processes.

The derived DSD parameters in Florence span similar values to Harvey and show a qualitatively similar joint probability distribution (Figure 9b). Some distinct differences are apparent, however, with a reduction in the spread of the observed DSD variability and a shift toward smaller drops (Figure 9c). The most common DSDs have an estimated D_0 at or below 1.0 mm, with relatively high number concentration. The overall similarity

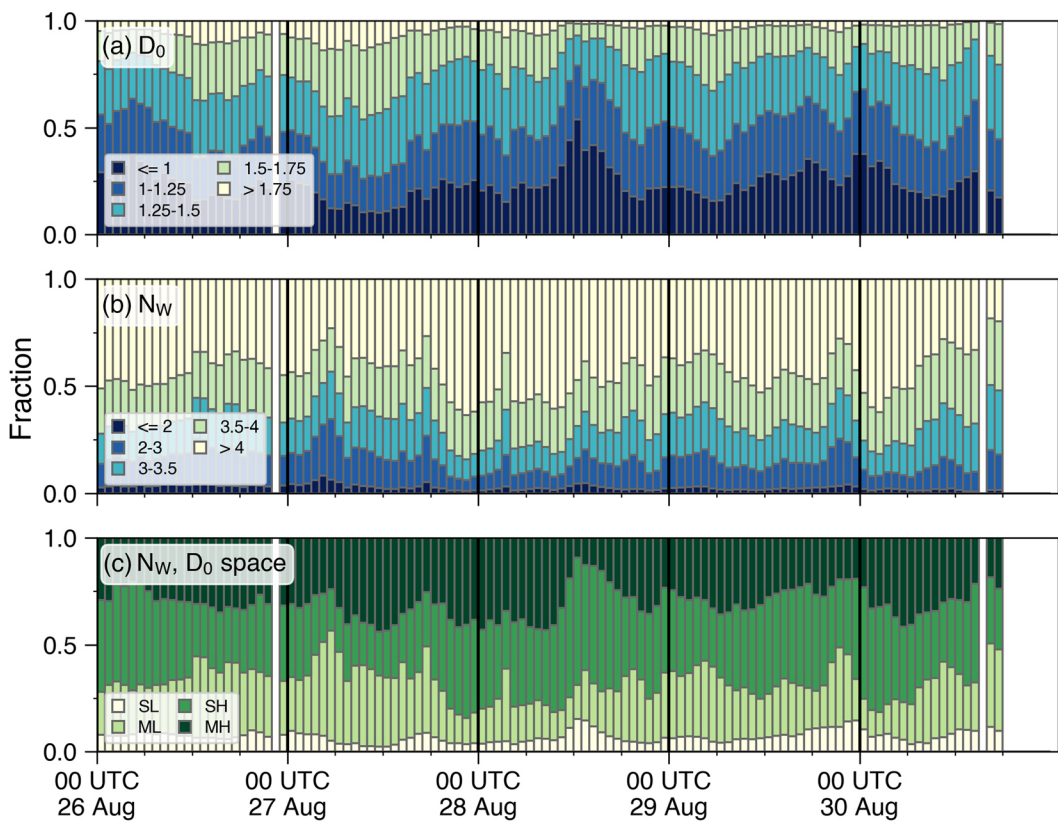


Figure 10. As in Figure 3, but for the estimated (a) D_0 (mm), (b) N_W (m^{-3} mm^{-1}), and (c) N_W, D_0 quadrants defined in Figure 9 for data from Harvey (2017).

between the Harvey and Florence probability distributions suggest comparable microphysical processes in general in both events but with more stronger convection in Harvey.

To provide more insight into the variability of the observed DSDs, we divide the joint N_W - D_0 distribution into four quadrants using boundaries of $3.5 \text{ m}^{-3} \text{ mm}^{-1}$ and 1.2 mm (Figure 9). These thresholds are arbitrary, but approximate the midpoint of each distribution. Not only does each quadrant have a different combination of median drop size and number concentration, but the thresholds separate the distributions by theoretical LWC values. In particular, the difference in the theoretical LWC between the lower-left (low LWC) and upper-right (high LWC) quadrants is substantial. The following quadrant descriptions are defined for the purposes of comparison: low-concentration small drops (quadrant SL), low-concentration medium drops (quadrant ML), high-concentration small drops (quadrant SH), and high-concentration medium drops (quadrant MH).

In Harvey, all four DSD quadrants coexisted over the radar domain at all times but their relative coverage varied in time (Figure 10). The fractional coverage of larger D_0 values achieved temporary maxima midday on 26 and 27 August and temporary minima midday on 28 August (Figure 10a). N_W variability over time was smaller than the variability in D_0 (Figure 10b). Although variable in time, the ML and SH quadrants are slightly more frequent throughout Harvey, while the SH quadrant is the most common (Figure 10c).

Overall, two notable regime shifts in the DSDs occurred during Harvey's evolution. First, a shift to larger drops occurred on 27 August, characterized by a maximum in D_0 values, increased quadrant MH coverage, and a maximum in quadrant ML coverage (Figure 10). At the same time, there is a shift to lower N_W values. These characteristics are consistent with the conclusions of Wolff et al. (2019) and Brauer et al. (2020). This regime was short lived, lasting only from 0400–01700 UTC on 27 August. The surge in medium drop coverage is similar to observations of a convective cell in an outer rainband in Typhoon Nida (2016) where bigger drops were prominent (Wu et al., 2018). In Wu et al. (2018), increased Z_H , Z_{DR} , and K_{DP} values were found beneath strong, deep ascent and high concentrations of graupel and aggregates, which indicated the

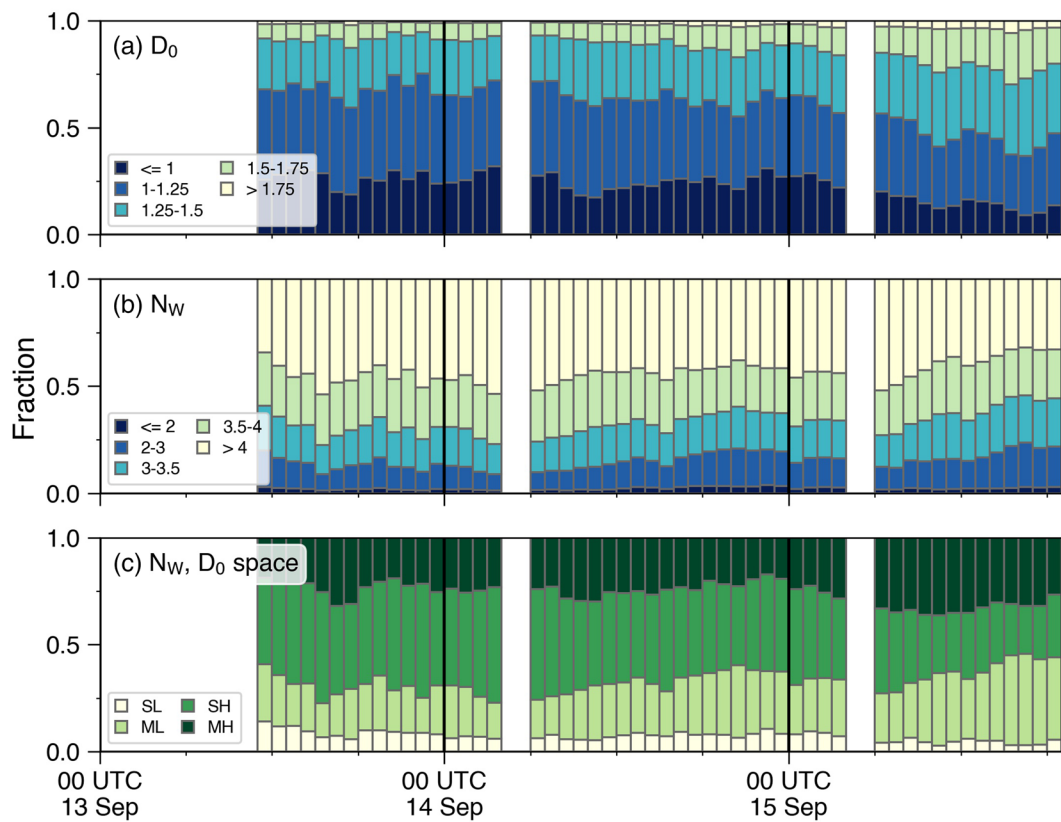


Figure 11. As in Figure 7, but for the estimated (a) D_0 (mm), (b) N_w ($m^{-3} \text{ mm}^{-1}$), and (c) N_w, D_0 quadrants defined in Figure 9 for data from Florence (2018).

importance of melting ice aloft to bigger raindrops below. Due to differences in methodology, it is unclear whether the drops in Nida (2016) would fall into our ML or MH quadrants. In the study by Wang et al. (2016) of Typhoon Matmo (2014), they did not observe a noticeable increase in low-concentration medium drops (our ML quadrant) but did report a shift toward higher number concentration (our MH quadrant) within a convective rainband. We note that the increase in medium drops observed by KHXG radar occurred around the same time that KIAH airport rain gauge was receiving its peak rain rates and the radar gates closest to the gauge showed a greater occurrence of the high-concentration drop quadrants (not shown). The fine-scale spatial and temporal variability confirms the challenge of TC precipitation forecasts to accurately predict local maxima embedded within a broad envelope of long duration light to moderate rain.

The second regime shift exhibited greater coverage by the high-concentration DSDs (SH and MH) during two periods: 1800 UTC on 27 August through 1200 UTC on 28 August and 0000-0600 UTC 30 August. In particular, the numerous, small drop DSDs (the SH quadrant) reached peak coverage. This smaller drop regime was noted by Wolff et al. (2019) on 28 August, although they did not analyze data from 30 August as the rain had exited Harris County. The prevalence of higher concentration of small-to-medium-sized drops is likely associated with an enhanced warm rain process. The extended period that rain was within range of the radar is a likely contributor to the large variety of near-surface microphysical characteristics compared to the Wang et al. (2016) and Wu et al. (2018) studies (4.5 days in the current study compared to less than 12 hours in the latter). The lengthy duration enabled multiple regions of the TC with different precipitation characteristics to pass over the radar.

The derived DSDs in Florence evolved more gradually than in Harvey, with reduced temporal variability but an increase in the medium drops (the ML and MH quadrants) that became more prominent after 0600 UTC on 15 September (Figure 11). The high number concentration DSDs (the SH and MH quadrants) have the greatest coverage, but the MH quadrant is less frequent than was seen for Harvey. The reduced frequency of the MH quadrant and increased frequency in the SH quadrant is due to generally weaker Z_H and Z_{DR} (cf. Figures 7a and 7b) and indicates a general shift to smaller drop sizes over time.

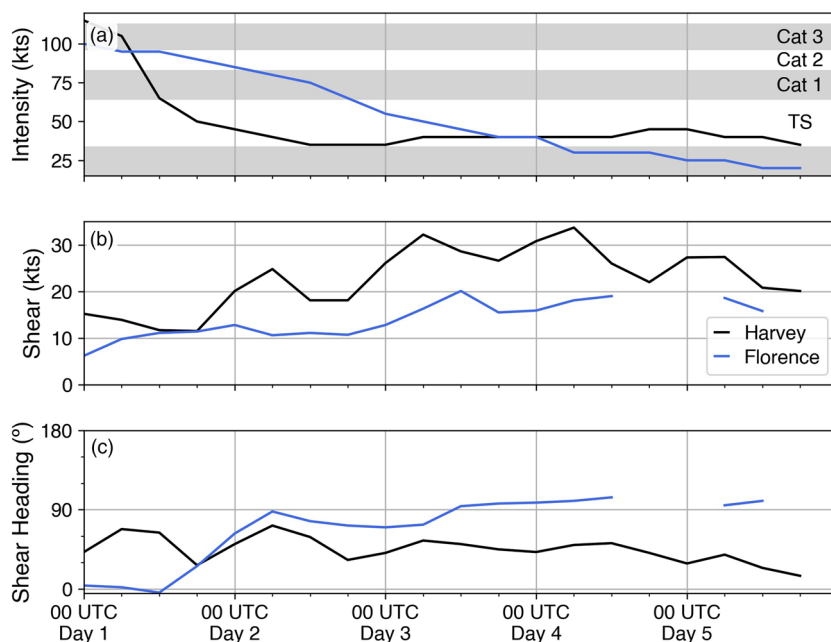


Figure 12. Time series of (a) storm intensity (kts), (b) deep-layer wind shear magnitude (kts), and (c) deep layer wind shear heading ($^{\circ}$) for Harvey (black) and Florence (blue). Label of Day 1 corresponds to 26 August and 13 September for Harvey and Florence, respectively.

Comparing the available data from Harvey and Florence reveals broad commonalities in microphysics of TC rainfall but important differences in the event length and local rain intensity. Harvey lingered over Texas for a longer amount of time and radar data indicate that the heaviest rain rates were more frequent and long-lasting than in Florence. Polarimetric data suggest both storms had a prevalence of small-to-medium-sized raindrops (≤ 2 mm) in moderate to high concentrations, but there was more temporal variability of the DSDs in Harvey than in Florence. We next examine some of the environmental and structural features that may have led to these differences.

5. Discussion

We hypothesize that several key factors were influential in producing the differences in observed rainfall in Harvey and Florence. First, Harvey and Florence had different intensities during their prolonged rain events. Although intensity does not directly correlate with storm structure, Harvey weakened more rapidly than Florence and spent more time as a tropical storm (Figure 12a). At the same time, the vertical wind shear surrounding Harvey was stronger than for Florence, which is known to produce azimuthal variations in precipitation. Deep-layer shear impacts vertical motion, and thus rainfall, in part by tilting the vortex. Vortex tilt induces a wavenumber-1 asymmetry of potential temperature, leading to persistent anomalies of isentropic ascent and descent (Jones, 1995). In addition, deep-layer shear imposes a wavenumber-1 pattern of radial flow and vorticity advection, which is roughly balanced by vortex compression or stretching (Bender, 1997).

As a weak storm under strong shear, Harvey was more asymmetric and disorganized. Initially, the strongest precipitation was found within convective outer rainbands that impacted the Houston metropolitan region (Figure 13a). The intense rainbands in Harvey share some similarities with the typhoon rainbands studied by Wang et al. (2016) and Wu et al. (2018) that indicated a prevalence of larger drops associated with stronger, deeper convective precipitation associated with “outer” rainbands (Tang et al., 2014, 2018; Yu & Tsai, 2013). One day later, hours after the center of Harvey reentered the Gulf of Mexico, precipitation weakened and became more scattered (Figure 13b). As Harvey moved northeast, the precipitation strengthened and became more uniform (Figure 13c). Finally, as the center of Harvey moved into Louisiana, the echo area was restricted to the region surrounding Beaumont, TX; the reduced echo area and higher reflectivity (Figure 13d) were associated with the resurgence of the heavy rain PID category and stronger polarimetric variables on 30 August (cf. Figures 2 and 3). Another notable feature in Harvey was the relative lack of

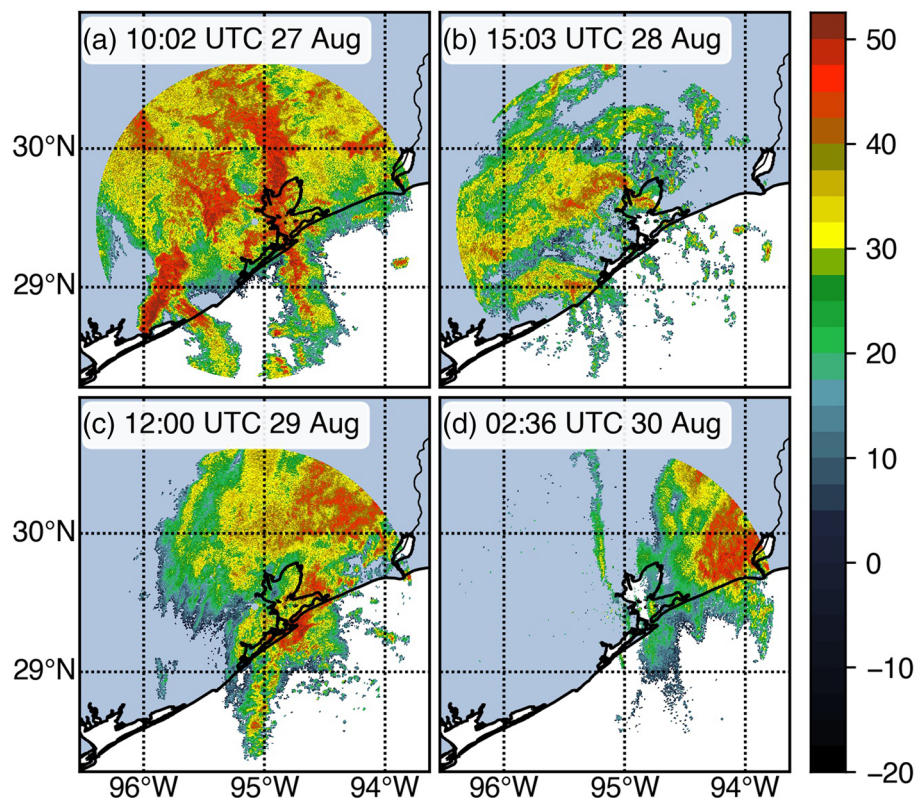


Figure 13. Map of reflectivity from the 0.5° PPI scan from KHXG at (a) 1002 UTC on 27 August, (b) 1503 UTC on 28 August, (c) 1200 UTC on 29 August, and (d) 0236 UTC on 30 August. Only data within 127 km of KHXG are displayed.

precipitation offshore. This structure suggests a strong influence of both onshore flow and persistent southwesterly shear. Under this shear orientation, southeast Texas spent a great deal of time in the downshear quadrants of Harvey, which are often characterized by enhanced overall rainfall, convective precipitation near the eyewall, and a transition from convective to stratiform precipitation in outer rainbands (Corbosiero & Molinari, 2002; DeHart et al., 2014; Hence & Houze, 2011, 2012; Reasor et al., 2013).

In contrast to Harvey's more asymmetric structure, we hypothesize that a slower decay rate and weaker shear favored a more resilient and axisymmetric structure for Florence. Increased rainfall axisymmetry is expected for stronger storms experiencing weaker deep-layer shear (Chen et al., 2006). The eyewall and rainbands

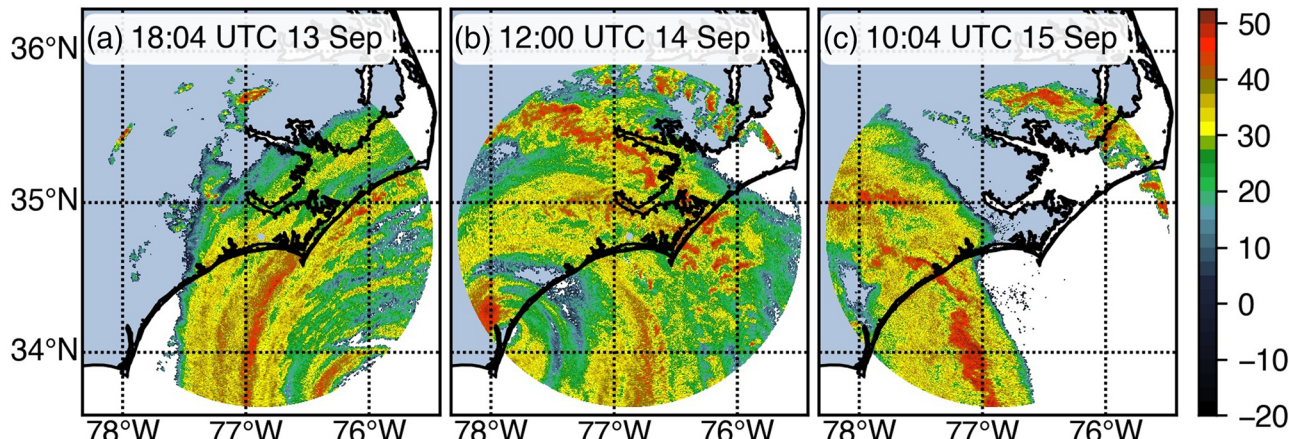


Figure 14. Map of reflectivity from the 0.5° PPI scan from KMHX at (a) 1804 UTC on 13 September, (b) 1200 UTC on 14 September, and (c) 1004 UTC on 15 September. Only data within 127 km of KMHX are displayed.

remained well-defined as Florence pushed through the KMHX domain (Figure 14). The heaviest rain in Florence was mostly restricted to the eyewall and inner rainbands, with larger areas of weaker reflectivity values and nonconvective precipitation similar to the inner rainband in Figure 8b. Unlike Harvey, heavy rainfall in Florence did not preferentially occur onshore. Although hints of heavier rainfall onshore exist in the eyewall and outer rainband on 14 September (Figure 14b), a band of heavier rainfall is present offshore on 15 September (Figure 14c). Determining which structures are due to processes associated with the coastal effects is challenging without numerical simulations, and should be a focus of further study.

During Florence's landfall, the shear direction veered from southerly to westerly through 0000 UTC on 14 September (Figure 12c), but the shear magnitude remained steady around 10 kts through 1800 UTC on 14 September. The concurrent axisymmetric structure suggests that Florence was more resilient to the influence of deep-layer shear. The relative axisymmetry of Florence during the slow decay was reflected in the persistent fractions of DSD types. The slow increase of large-sized DSDs coincided with Florence's departure from the radar domain as a solitary rainband dominated the remaining precipitating area (Figure 14c). Since different TC features exhibit different types of DSDs (Tang et al., 2014, 2018; Wang et al., 2016; Wu et al., 2018; Yu & Tsai, 2013), a gradual transition from a regime that includes eyewall, inner rainband, and outer rainband rainfall (e.g., 14 September in Figure 14b) to predominantly outer rainband rainfall likely contributes to the changing DSD type fractions. Overall, the polarimetric data suggest that strong convection was less widespread in Florence than in Harvey. The stronger TC intensity and resilience to deep-layer shear are believed to limit the intense convection to smaller areas in the eyewall and rainbands compared to the stronger vertical motion forcing downshear in Harvey.

Vertical wind shear and intensity are not the only possible factors that could explain the difference in precipitation between the two storms. Environmental conditions such as dry air, thermodynamic stability, and sea surface temperatures also affect cloud morphology and the resulting precipitation. Offshore sea surface temperatures in the Gulf of Mexico prior to Harvey were approximately 1° C warmer than offshore temperatures for Florence (not shown) and could have increased low-level moisture in Harvey. While these factors may also play a role, the contrasting storm structures and consistency with expected patterns of precipitation due to vertical wind shear suggest that the combined effects of shear and intensity played an important role in the rainfall differences. Further analysis with high-resolution thermodynamic observations and numerical simulations would be required to evaluate their relative contributions and are beyond the scope of this study.

6. Conclusions

In this study, rain gauge and polarimetric radar data were analyzed to better understand the characteristics of the record-setting rainfall from Hurricanes Harvey (2017) and Florence (2018) and to identify microphysical similarities and differences between these two storms. From our analysis, we draw the following conclusions:

1. Polarimetric data indicated that the microphysical characteristics of both storms were not drastically different from the observations in previous TCs. On average, both Harvey and Florence exhibited 'typical' TC DSDs with high concentrations of small-to-medium-sized raindrops.
2. High-concentration, midsize DSDs were more common in Harvey and indicate stronger rain rates over a larger area for a longer time period. The dominant DSD type (e.g., large N_W or D_0 DSDs) in Harvey showed substantial variability over time. In contrast, inferred DSDs from Florence generally had smaller median diameters than the DSDs from Harvey and had less variability.
3. Both the long event duration and strong rain rates were contributing factors to the record-breaking rainfall in Harvey, but their relative importance varied spatially. The slowly moving center determined the amount of time any one location spent in onshore flow and was one of the primary contributors to the frequency of heavy rain rates and the record-breaking total accumulated rainfall. In contrast, Florence's more direct track and shorter duration did not produce as distinct a difference in on- and offshore precipitation or the spatial or temporal variability in intense rain rates.
4. Stronger vertical wind shear and a more rapid decay in intensity contributed to a more asymmetric and disorganized Harvey, whereas weaker wind shear and a slower decay in intensity contributed to a

more resilient and axisymmetric Florence. These factors contribute to overall weaker convection in Florence associated with “inner” rainbands, while Harvey’s stronger convection more resembled “outer” rainbands.

It is well known that slow-moving TCs are capable of producing extreme rainfall, but this study further underscores the complexity inherent in TC rainfall. Rain rates and the dominant microphysical processes vary sharply over short distances, depend on the details of the TC structure, and are influenced by the environment. The changing DSDs in Harvey and Florence suggests changes in the relative contributions of rain and ice phase processes, consistent with previous TC studies (Didlake & Kumjian, 2017; Kalina et al., 2017; Wang et al., 2016; Wu et al., 2018). Abundant small drops suggest the dominance of warm rain processes, while the presence of larger drops suggest more vigorous or deeper convection with more contributions from melting graupel to the overall DSD (Wu et al., 2018). The current results suggest that multiple microphysical pathways to heavy rainfall exist within the same TC, and additional research is needed to determine which pathways will dominate in different regions and landfall scenarios.

Understanding the key factors in specific extreme rainfall events can help identify commonalities and differences in future extreme events. Recent studies suggest that TC rainfall is expected to increase in a warmer climate, and that climate change may have influenced Harvey’s rainfall through increased water vapor, higher ocean heat content, or slower storm motion (Emanuel, 2017; Risser & Wehner, 2017; Trenberth et al., 2018; van Oldenborgh et al., 2017). While the role of climate change in the two events presented here is outside the scope of this study, documenting the characteristics of their rainfall is crucial to understanding how such characteristics might change in the future. In particular, the relative spatial and temporal contributions of various microphysical processes to the total rainfall are not fully understood. A specific process might be an efficient producer of strong precipitation, but may have a limited impact in the context of the full event and area of impact. Concurrent surface, in situ, and remote observations of microphysical processes will improve our understanding of and ability to forecast TC rainfall in the current and future climate.

Acknowledgments

This study was supported by the National Science Foundation Awards AGS-1701225, AGS-1854607, and OAC-1661663. The authors would like to thank Ya-Chien Feng for her comments on the manuscript. The authors would also like to thank the three anonymous reviewers, whose comments helped improve this manuscript. The WSR-88D Level II radar data can be obtained from the National Climatic Data Center (<https://www.ncdc.noaa.gov/nexradinv>). The hourly rain gauge data can be obtained from the ASOS archive maintained by the Iowa Environmental Mesonet (<https://mesonet.agron.iastate.edu/request/download.phtml>). The LROSE software is available for download online (<https://lrose.net>).

References

- Bell, M. M. (2019). nsf-lrose/lrose-blaze: lrose-blaze-20190105, <https://doi.org/10.5281/ZENODO.2532758>
- Bender, M. A. (1997). The effect of relative flow on the asymmetric structure in the interior of hurricanes. *Journal of the Atmospheric Sciences*, 54(6), 703–724. [https://doi.org/10.1175/1520-0469\(1997\)054<0703:TEORFO>2.0.CO;2](https://doi.org/10.1175/1520-0469(1997)054<0703:TEORFO>2.0.CO;2)
- Black, R. A., & Hallett, J. (1986). Observations of the distribution of ice in hurricanes. *Journal of the Atmospheric Sciences*, 43(8), 802–822. [https://doi.org/10.1175/1520-0469\(1986\)043<0802:OOTDOI>2.0.CO;2](https://doi.org/10.1175/1520-0469(1986)043<0802:OOTDOI>2.0.CO;2)
- Black, R. A., & Hallett, J. (1999). Electrification of the hurricane. *Journal of the Atmospheric Sciences*, 56(12), 2004–2028.
- Blake, E. S., & Zelinsky, D. A. (2018). Tropical cyclone report: Hurricane Harvey (17 August–1 September 2017: National Hurricane Center, National Oceanographic and Atmospheric Administration.
- Brandes, E. A., Zhang, G., & Vivekanandan, J. (2004). Drop size distribution retrieval with polarimetric radar: Model and application. [https://doi.org/10.1175/1520-0450\(2004\)043<0461:DSDRWP>2.0.CO;2](https://doi.org/10.1175/1520-0450(2004)043<0461:DSDRWP>2.0.CO;2)
- Brauer, N. S., Basara, J. B., Homeyer, C. R., McFarquhar, G. M., & Kirstetter, P. E. (2020). Quantifying precipitation efficiency and drivers of excessive precipitation in post-landfall Hurricane Harvey. *Journal of Hydrometeorology*, 21, 433–452. <https://doi.org/10.1175/jhm-d-19-0192.1>
- Bringi, V. N., & Chandrasekar, V. (2001). *Polarimetric Doppler weather radar* (Vol. 136, pp. 636). Cambridge University Press. <https://doi.org/10.1017/cbo9780511541094>
- Bringi, V. N., Chandrasekar, V., Hubbert, J., Gorgucci, E., Randeu, W. L., Schoenhuber, M., et al. (2003). Raindrop size distribution in different climatic regimes from disdrometer and dual-polarized radar analysis. *Journal of the Atmospheric Sciences*, 60(2), 354–365. [https://doi.org/10.1175/1520-0469\(2003\)060<0354:RSDIDC>2.0.CO;2](https://doi.org/10.1175/1520-0469(2003)060<0354:RSDIDC>2.0.CO;2)
- Bringi, V. N., Tolstoy, L., Thurai, M., & Petersen, W. A. (2015). Estimation of spatial correlation of drop size distribution parameters and rain rate using NASA’s S-band polarimetric radar and 2D video disdrometer network: Two case studies from MC3e. *Journal of Hydrometeorology*, 16(3), 1207–1221. <https://doi.org/10.1175/JHM-D-14-0204.1>
- Brown, B. R., Bell, M. M., & Frambah, A. J. (2016). Validation of simulated hurricane drop size distributions using polarimetric radar. *Geophysical Research Letters*, 43, 910–917. <https://doi.org/10.1002/2015GL067278>
- Chang, W. Y., Wang, T. C. C., & Lin, P. L. (2009). Characteristics of the raindrop size distribution and drop shape relation in typhoon systems in the western pacific from the 2D video disdrometer and NCU C-band polarimetric radar. *Journal of Atmospheric and Oceanic Technology*, 26(10), 1973–1993. <https://doi.org/10.1175/2009JTECHA1236.1>
- Chen, S. S., Knaff, J. A., & Marks, F. D. (2006). Effects of vertical wind shear and storm motion on tropical cyclone rainfall asymmetries deduced from TRMM. *Monthly Weather Review*, 134(11), 3190–3208. <https://doi.org/10.1175/MWR3245.1>
- Corbosiero, K. L., & Molinari, J. (2002). The effects of vertical wind shear on the distribution of convection in tropical cyclones. *Monthly Weather Review*, 130(8), 2110–2123. [https://doi.org/10.1175/1520-0493\(2002\)130<2110:TEOVWS>2.0.CO;2](https://doi.org/10.1175/1520-0493(2002)130<2110:TEOVWS>2.0.CO;2)
- Cunningham, J. G., Zittel, W. D., Lee, R. R., Ice, R. L., & Hoban, N. P. (2013). Methods for identifying systematic differential reflectivity (Zdr) biases on the operational WSR-88D network. *36th Conference on Radar Meteorology*, 9, 1–24.
- DeHart, J. C., Houze, R. A., & Rogers, R. F. (2014). Quadrant distribution of tropical cyclone inner-core kinematics in relation to environmental shear. *Journal of the Atmospheric Sciences*, 71(7), 2713–2732. <https://doi.org/10.1175/JAS-D-13-0298.1>
- DeMaria, M., Mainelli, M., Shay, L. K., Knaff, J. A., & Kaplan, J. (2005). Further improvements to the statistical hurricane intensity prediction scheme (SHIPS). *Bulletin of the American Meteorological Society*, 86(9), 1217. <https://doi.org/10.1175/WAF862.1>

- Didlake, A. C., & Kumjian, M. R. (2017). Examining polarimetric radar observations of bulk microphysical structures and their relation to vortex kinematics in Hurricane Arthur (2014). *Monthly Weather Review*, 145(11), 4521–4541. <https://doi.org/10.1175/MWR-D-17-0035.1>
- Didlake, A. C., & Kumjian, M. R. (2018). Examining storm asymmetries in Hurricane Irma (2017) using polarimetric radar observations. *Geophysical Research Letters*, 45, 13,513–13,522. <https://doi.org/10.1029/2018GL080739>
- Emanuel, K. (2017). Assessing the present and future probability of Hurricane Harvey's rainfall. *Proceedings of the National Academy of Sciences of the United States of America*, 114(48), 12,681–12,684. <https://doi.org/10.1073/pnas.1716222114>
- Feng, Y. C., & Bell, M. M. (2019). Microphysical characteristics of an asymmetric eyewall in major Hurricane Harvey (2017). *Geophysical Research Letters*, 46, 461–471. <https://doi.org/10.1029/2018GL080770>
- Hence, D. A., & Houze, R. A. (2011). Vertical structure of hurricane eyewalls as seen by the TRMM precipitation radar. *Journal of the Atmospheric Sciences*, 68(8), 1637–1652. <https://doi.org/10.1175/2011JAS3578.1>
- Hence, D. A., & Houze, R. A. (2012). Vertical structure of tropical cyclone rainbands as seen by the TRMM precipitation radar. *Journal of the Atmospheric Sciences*, 69(9), 2644–2661. <https://doi.org/10.1175/JAS-D-11-0323.1>
- Hitchens, N. M., Brooks, H. E., & Schumacher, R. S. (2013). Spatial and temporal characteristics of heavy hourly rainfall in the United States. *Monthly Weather Review*, 141(12), 4564–4575. <https://doi.org/10.1175/MWR-D-12-00297.1>
- Houze, R. A., Marks, F. D., & Black, R. A. (1992). Dual-aircraft investigation of the inner core of Hurricane Norbert. Part II: Mesoscale distribution of ice particles. [https://doi.org/10.1175/1520-0469\(1992\)049<0943:DAIOTI>2.0.CO;2](https://doi.org/10.1175/1520-0469(1992)049<0943:DAIOTI>2.0.CO;2)
- Hubert, J., & Bringi, V. N. (1995). An iterative filtering technique for the analysis of copolar differential phase and dual-frequency radar measurements. *Journal of Atmospheric and Oceanic Technology*, 12(3), 643–648. [https://doi.org/10.1175/1520-0426\(1995\)012<0643:aiftft>2.0.co;2](https://doi.org/10.1175/1520-0426(1995)012<0643:aiftft>2.0.co;2)
- Jones, S. C. (1995). The evolution of vortices in vertical shear. I: Initially barotropic vortices. *Quarterly Journal of the Royal Meteorological Society*, 121(524), 821–851. <https://doi.org/10.1002/qj.49712152406>
- Jorgensen, D. P., & Willis, P. T. (1982). A Z-R Relationship for Hurricanes. *Journal of Applied Meteorology*, 21(3), 356–366. [https://doi.org/10.1175/1520-0450\(1982\)021<0356:azrfrh>2.0.co;2](https://doi.org/10.1175/1520-0450(1982)021<0356:azrfrh>2.0.co;2)
- Kalina, E. A., Matrosov, S. Y., Cione, J. J., Marks, F. D., Vivekanandan, J., Black, R. A., et al. (2017). The ice water paths of small and large ice species in Hurricanes Arthur (2014) and Irene (2011). *Journal of Applied Meteorology and Climatology*, 56(5), 1383–1404. <https://doi.org/10.1175/JAMC-D-16-0300.1>
- Kumjian, M. (2013). Principles and applications of dual-polarization weather radar. Part I: Description of the polarimetric radar variables. *Journal of Operational Meteorology*, 1(19), 226–242. <https://doi.org/10.15191/nwajom.2013.0119>
- Kumjian, M. R., & Prat, O. P. (2014). The impact of raindrop collisional processes on the polarimetric radar variables. *Journal of the Atmospheric Sciences*, 71(8), 3052–3067. <https://doi.org/10.1175/JAS-D-13-0357.1>
- Lang, T., Dolan, B., Guy, N., Gerlach, C., & Hardin, J. (2019). CSU-Radarmet/CSU_RadarTools: CSU_RadarTools, v1, 3. <https://doi.org/10.5281/ZENODO.2562063>
- Marks, F. D., & Houze, R. A. (1987). Inner core structure of Hurricane Alicia from airborne Doppler radar observations. *Journal of the Atmospheric Sciences*, 44(9), 1296–1317. [https://doi.org/10.1175/1520-0469\(1987\)044<1296:ICSOHA>2.0.CO;2](https://doi.org/10.1175/1520-0469(1987)044<1296:ICSOHA>2.0.CO;2)
- Rappaport, E. N. (2014). Fatalities in the United States from atlantic tropical cyclones: New data and interpretation. *Bulletin of the American Meteorological Society*, 95(3), 341–346. <https://doi.org/10.1175/BAMS-D-12-00074.1>
- Reasor, P. D., Rogers, R., & Lorsolo, S. (2013). Environmental flow impacts on tropical cyclone structure diagnosed from airborne doppler radar composites. *Monthly Weather Review*, 141(9), 2949–2969. <https://doi.org/10.1175/MWR-D-12-00334.1>
- Risser, M. D., & Wehner, M. F. (2017). Attributable human-induced changes in the likelihood and magnitude of the observed extreme precipitation during Hurricane Harvey. *Geophysical Research Letters*, 44, 12,457–12,464. <https://doi.org/10.1002/2017GL075888>
- Ryzhkov, A. V., Schuur, T. J., Burgess, D. W., Heinselman, P. L., Giangrande, S. E., & Zrnic, D. S. (2005). The joint polarization experiment: Polarimetric rainfall measurements and hydrometeor classification. <https://doi.org/10.1175/BAMS-86-6-809>
- Ryzhkov, A. V., & Zrnic, D. S. (2019). Radar polarimetry for weather observations. <https://doi.org/10.1007/978-3-030-05093-1>
- Stewart, S. R., & Berg, R. (2019). Tropical cyclone report: Hurricane Florence (31 August–17 September 2018: National Hurricane Center, National Oceanographic and Atmospheric Administration.
- Tang, X., Lee, W. C., & Bell, M. (2014). A squall-line-like principal rainband in Typhoon Hagupit (2008) observed by airborne Doppler radar. *Journal of the Atmospheric Sciences*, 71(7), 2733–2746. <https://doi.org/10.1175/JAS-D-13-0307.1>
- Tang, X., Lee, W. C., & Bell, M. (2018). Subrainband structure and dynamic characteristics in the principal rainband of Typhoon Hagupit (2008). *Monthly Weather Review*, 146(1), 157–173. <https://doi.org/10.1175/MWR-D-17-0178.1>
- Thompson, E. J., Rutledge, S. A., Dolan, B., & Thurai, M. (2015). Drop size distributions and radar observations of convective and stratiform rain over the equatorial Indian and West Pacific Oceans. *Journal of the Atmospheric Sciences*, 72(11), 4091–4125. <https://doi.org/10.1175/JAS-D-14-0206.1>
- Thompson, E. J., Rutledge, S. A., Dolan, B., Thurai, M., & Chandrasekar, V. (2018). Dual-polarization radar rainfall estimation over tropical oceans. *Journal of Applied Meteorology and Climatology*, 57(3), 755–775. <https://doi.org/10.1175/JAMC-D-17-0160.1>
- Tokay, A., Bashor, P. G., Habib, E., & Kapsaris, T. (2008). Raindrop size distribution measurements in tropical cyclones. *Monthly Weather Review*, 136(5), 1669–1685. <https://doi.org/10.1175/2007MWR2122.1>
- Trenberth, K. E., Cheng, L., Jacobs, P., Zhang, Y., & Fasullo, J. (2018). Hurricane Harvey links to ocean heat content and climate change adaptation. *Earth's Future*, 6(5), 730–744. <https://doi.org/10.1029/2018EF000825>
- Ulbrich, C. W. (1983). Natural variations in the analytical form of the raindrop size distribution. *Journal of Climate and Applied Meteorology*, 22(10), 1764–1775. [https://doi.org/10.1175/1520-0450\(1983\)022<1764:NVITAF>2.0.CO;2](https://doi.org/10.1175/1520-0450(1983)022<1764:NVITAF>2.0.CO;2)
- Ulbrich, C. W., & Lee, L. G. (2002). Rainfall characteristics associated with the remnants of tropical Storm Helene in upstate South Carolina. *Weather and Forecasting*, 17(6), 1257–1267. [https://doi.org/10.1175/1520-0434\(2002\)017<1257:rcaawt>2.0.co;2](https://doi.org/10.1175/1520-0434(2002)017<1257:rcaawt>2.0.co;2)
- van Oldenborgh, G. J., van der Wiel, K., Sebastian, A., Singh, R., Arrighi, J., Otto, F., et al. (2017). Attribution of extreme rainfall from Hurricane Harvey, August 2017. *Environmental Research Letters*, 12(12), 124,009. <https://doi.org/10.1088/1748-9326/aa9ef2>
- Vivekanandan, J., Zrnic, D. S., Ellis, S. M., Oye, R., Ryzhkov, A. V., & Straka, J. (1999). Cloud microphysics retrieval using S-band dual-polarization radar measurements. *Bulletin of the American Meteorological Society*, 80(3), 381–388. [https://doi.org/10.1175/1520-0477\(1999\)080<0381:CMRUSB>2.0.CO;2](https://doi.org/10.1175/1520-0477(1999)080<0381:CMRUSB>2.0.CO;2)
- Wang, M., Zhao, K., Xue, M., Zhang, G., Liu, S., Wen, L., & Chen, G. (2016). Precipitation microphysics characteristics of a Typhoon Matmo (2014) rainband after landfall over eastern China based on polarimetric radar observations. *Journal of Geophysical Research: Atmospheres*, 121, 12,415–12,433. <https://doi.org/10.1002/2016JD025307>
- Willis, P. T. (1984). Functional fits to some observed drop size distributions and parameterization of rain. *Journal of the Atmospheric Sciences*, 41(9), 1648–1661. [https://doi.org/10.1175/1520-0469\(1984\)041<1648:FFTSOD>2.0.CO;2](https://doi.org/10.1175/1520-0469(1984)041<1648:FFTSOD>2.0.CO;2)

- Wolff, D. B., Petersen, W. A., Tokay, A., Marks, D. A., & Pippitt, J. L. (2019). Assessing dual-polarization radar estimates of extreme rainfall during Hurricane Harvey. *Journal of Atmospheric and Oceanic Technology*, 36, 2501–2520. <https://doi.org/10.1175/JTECH-D-19-0081.1>
- Wu, D., Zhao, K., Kumjian, M. R., Chen, X., Huang, H., Wang, M., et al. (2018). Kinematics and microphysics of convection in the outer rainband of Typhoon Nida (2016) revealed by polarimetric radar. *Monthly Weather Review*, 146(7), 2147–2159. <https://doi.org/10.1175/MWR-D-17-0320.1>
- Yu, C. K., & Tsai, C. L. (2013). Structural and surface features of arc-shaped radar echoes along an outer tropical cyclone rainband. *Journal of the Atmospheric Sciences*, 70(1), 56–72. <https://doi.org/10.1175/JAS-D-12-090.1>
- Zagrodnik, J. P., McMurdie, L. A., & Houze, R. A. (2018). Stratiform precipitation processes in cyclones passing over a coastal mountain range. *Journal of the Atmospheric Sciences*, 75(3), 983–1004. <https://doi.org/10.1175/JAS-D-17-0168.1>
- Zhang, G., Vivekanandan, J., & Brandes, E. (2001). A method for estimating rain rate and drop size distribution from polarimetric radar measurements. *IEEE Transactions on Geoscience and Remote Sensing*, 39(4), 830–841. <https://doi.org/10.1109/36.917906>